Effects of spanwise confinement on stratified shear instabilities

Yves-Marie Ducimetière [*] and François Gallaire
Laboratory of Fluid Mechanics and Instabilities, EPFL, CH1015 Lausanne, Switzerland

Adrien Lefauve and Colm-cille P. Caulfield [†]
Department of Applied Mathematics and Theoretical Physics, University of Cambridge,
Centre for Mathematical Sciences, Wilberforce Road, Cambridge CB3 0WA, United Kingdom

We consider the influence of transverse confinement on the instability properties of velocity and density distributions reminiscent of those pertaining to exchange flows in stratified inclined ducts, such as the recent experiment of Lefauve *et al.* [J. Fluid Mech. **848**, 508 (2018)]. Using a normal mode streamwise and temporal expansion for flows in ducts with various aspect ratios B and nontrivial transverse velocity profiles, we calculate two-dimensional (2D) dispersion relations with associated eigenfunctions varying in the "crosswise" direction, in which the density varies, and the spanwise direction, both normal to the duct walls and to the flow direction. We also compare these 2D dispersion relations to the so-called one-dimensional (1D) dispersion relations obtained for spanwise invariant perturbations, for different aspect ratios B and bulk Richardson numbers Ri_b. In this limited parameter space, the presence of lateral walls has a stabilizing effect, in that the 1D growth-rate predictions are almost systematically an upper bound to the 2D growth rates, which in turn decrease monotonically as lateral walls are brought together with increased spanwise confinement ($B \to 0$). Furthermore, accounting for spanwise-varying perturbations results in a plethora of unstable modes, the number of which increases as the aspect ratio is increased. These modes present an odd-even regularity in their spatial structures, which is rationalized by comparison to the so-called one-dimensional oblique dispersion relation obtained for oblique waves, characterized by a continuously varying spanwise wavenumber in addition to the streamwise wavenumber. Finally, we show that in most cases, the most unstable 2D mode is the one that oscillates the least in the spanwise direction, as a consequence of viscous damping. However, in a limited region of the parameter space and in the absence of stratification, we show that a secondary mode with a more complex "twisted" structure dominated by crosswise vorticity becomes more unstable than the least oscillating Kelvin-Helmholtz mode associated with spanwise vorticity.

I. INTRODUCTION

Flows in the natural environment (such as in the atmosphere or ocean) are often stably stratified in the vertical, with the horizontally averaged density decreasing with height. Such environmental flows are also often characterized by a background velocity distribution that decreases with height, resulting in vertical shear. This combined effect of buoyancy and shear results in a large variety

---

[*]yves-marie.ducimetiere@epfl.ch
[†]Also at BP Institute, University of Cambridge, Madingley Road, Cambridge CB3 0EZ, United Kingdom.

of interesting dynamical behaviors exhibited by stratified shear flows. An important ingredient influencing such behaviors is the spatial confinement, inherent to many geophysical flows such as valleys, estuaries [1], submarine canyons, straits, or deep ocean trenches.

Perhaps the most classical example of this dynamical behavior is the overturning Kelvin-Helmholtz instability (perhaps more appropriately called a Rayleigh instability when the region of inflectional shear has a finite depth) as well as so-called Holmboe instabilities, typically associated with relatively "sharp" density gradients, which all contribute to the mixing and transport of heat, salt, or indeed various pollutants. In the Kelvin-Helmholtz instability, a single instability mode appears, traveling at the mean velocity of the fluid layer, which can grow into an array of elliptical vortical billows, that in turn overturn and smear out the density interface. In contrast, the Holmboe instability gives rise to propagating modes, which are associated (at finite amplitude) with vortices displaced from the density interface, which typically survives the ensuing scouring motion.

The Holmboe instability has attracted in recent years a large variety of numerical and experimental studies. Direct numerical simulations (DNSs) have enabled a thorough description of nonlinear saturation and mixing mechanisms [2–7]. Laboratory experiments have been conducted in salt-stratified exchange flows that also investigate various aspects of this instability [8–11]. In particular, Ref. [12] investigates the laboratory-scale realization of the Holmboe instability. A sustained stratified shear flow is generated in the laboratory by exchange flow through an inclined square duct, connecting two reservoirs filled with fluids of different densities. The duct confines the flow in the "crosswise" direction (slightly tilted from the vertical) along which it is stratified, as well as in the spanwise direction.

In Ref. [12], a three-dimensional, nonlinear, and asymmetric Holmboe wave (in this context the finite amplitude manifestation of the instability) was observed and characterized in detail using three-dimensional, volumetric measurements of the velocity and density fields. A temporal local linear stability analysis on the two-dimensional, streamwise-averaged, experimental flow was also performed. Three-dimensional perturbations were sought, having two-dimensional, cross-sectionally confined eigenfunctions and a streamwise normal mode expansion. The matching between the resulting most unstable eigenmode developing on the mean flow and the experimental structure proved to be (perhaps surprisingly) excellent, validating the *a posteriori* linear stability approach, where the time-averaged flow used captured the nonlinear effects of the various perturbations.

Of great interest in Ref. [12] is the importance of the spanwise confinement to the dynamical evolution of the Holmboe wave. With v and ω designating the spanwise velocity and vorticity, respectively, they observed that the presence of lateral walls "gives rise to relatively large spanwise gradients $|\partial_y v|$, positive in the centre of the duct and negative near the boundaries. These gradients have a vortex stretching effect on ω_y [. . .] producing negative vorticity in the centre (reinforcing the mean shear), and positive vorticity near the boundaries (weakening the mean shear)" (p. 534). As mentioned previously, such a strong confinement effect should also be present in many geophysical flows. In this context, Ref. [12] also draws attention to the fact that "laboratory observations in confined geometries are often compared to stability analyses that ignore confinement, and numerical simulations usually impose periodic boundary conditions in the spanwise direction" (p. 540). The extent to which properties of three-dimensional confined (in the transverse, along-crest direction) waves are well predicted by such analyses is difficult to predict *a priori*, and remains an open question. We aim to address this question here, considering a flow configuration motivated by the experimental geometry described in Ref. [12].

To address this aim, we will proceed as follows. In Sec. II, we describe our linear two-dimensional (2D) stability analysis and recall some fundamental results from the related literature. In Sec. III, dispersion relations of the most unstable confined modes are presented in selected parameter space; they are compared to classical one-dimensional (1D) (in the sense of being spanwise invariant) predictions. In Sec. IV, we restrict ourselves to a particular wavenumber and analyze in greater detail the unstable part of the spectrum. We compare the associated predictions to generalized 1D predictions, allowing oblique modes. In Sec. V, we analyze in detail a specific
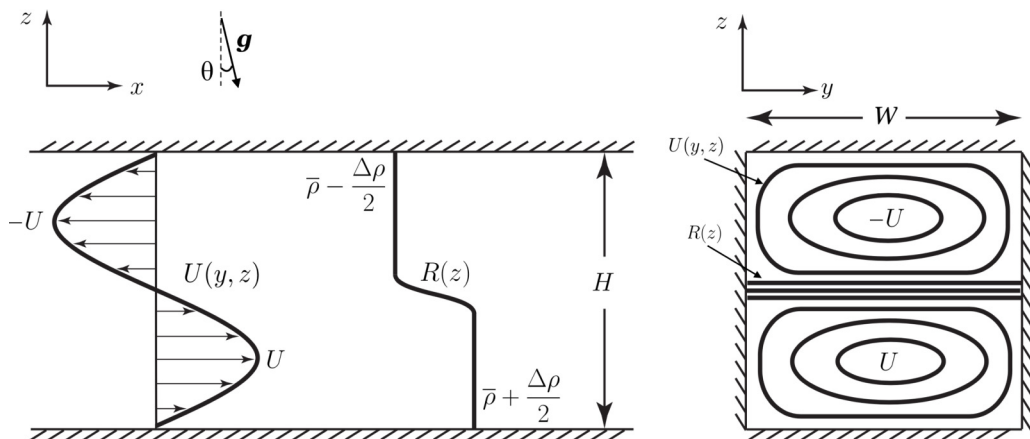
FIG. 1. Schematic of our confined duct flow configuration (dimensional variables).

mode that appears actually to be destabilized by the presence of transverse walls. Finally, we draw some relatively brief conclusions, and suggest potential further directions of research.

II. PROBLEM FORMULATION, BACKGROUND, AND OBJECTIVES

A. Formulation

1. Flow configuration and notations

The flow configuration is illustrated in Fig. 1. The streamwise (x) axis is aligned along the duct, the spanwise (y) axis is across it, and the crosswise (z) axis is tilted at an angle θ from the true vertical, resulting in a nonzero projection of the gravity driving the exchange flow in the streamwise direction. The duct is assumed infinitely long in the streamwise direction to avoid end effects. The coordinate system is centered in the middle of the duct cross section, such that $-H/2 \leqslant z \leqslant H/2$ and $-W/2 \leqslant y \leqslant W/2$, where H is the duct crosswise "height" and W the duct spanwise "width." The velocity field is $\mathbf{u}(x, y, z, t) = (u, v, w)$, the density field is $\rho(x, y, z, t)$, and the pressure field is $p(x, y, z, t)$. The base velocity profile $U(y, z)$ and density profile $\mathcal{R}(z)$ will be specified in Sec. II A 3.

To nondimensionalize the problem we choose to scale velocities by half the total (peak-to-peak) velocity jump in the base flow, $(\tilde{u}, \tilde{v}, \tilde{w}) = (u, v, w)/(\Delta U/2)$, and lengths by half the height of the duct, $(\tilde{x}, \tilde{y}, \tilde{z}) = (x, y, z)/(H/2)$, such that $-1 \leqslant \tilde{z} \leqslant 1$ and $-B \leqslant \tilde{y} \leqslant B$, where

$$B = \frac{W}{H} \tag{1}$$

is the duct aspect ratio; $B < 1$ corresponds to what we refer to as a "narrow" duct, $B = 1$ to a square duct, and $B > 1$ corresponds to what we refer to as a wide duct. The corresponding nondimensional advective time is $\tilde{t} = t/(H/\Delta U)$. Finally, the nondimensional density is $\tilde{\rho} = (\rho - \rho_0)/(\Delta\rho/2)$, where ρ_0 is the mean reference value and $\Delta\rho/2$ is half the (peak-to-peak) density jump in the density base profile.

2. Governing equations

We model the flow by the incompressible Navier-Stokes equations under the Boussinesq approximation, which requires $\Delta\rho/\rho_0 \ll 1$ (valid for the experimental flow configuration of Ref. [12]); i.e., the density difference only plays a role through the reduced gravity $g' = g\Delta\rho/\rho_0$. In addition,

the kinematic viscosity (ν) and the mass (salt) diffusivity (κ_m) are assumed constant. Dropping the tildes, we obtain the following set of nondimensional governing equations:

$$\boldsymbol{\nabla} \cdot \mathbf{u} = 0, \tag{2a}$$

$$\partial_t \mathbf{u} + \mathbf{u} \cdot \boldsymbol{\nabla} \mathbf{u} = -\boldsymbol{\nabla} p + \mathrm{Ri}_b(-\cos\theta\hat{\mathbf{z}} + \sin\theta\hat{\mathbf{x}})\rho + \mathrm{Re}^{-1}\boldsymbol{\Delta}\mathbf{u}, \tag{2b}$$

$$\partial_t \rho + \mathbf{u} \cdot \boldsymbol{\nabla} \rho = (\mathrm{Re}\,\mathrm{Sc})^{-1}\boldsymbol{\Delta}\rho, \tag{2c}$$

where the nondimensional parameters are

$$\mathrm{Re} = \frac{\Delta U H}{4\nu}, \quad \mathrm{Ri}_b = \frac{g\Delta\rho H}{\rho_0(\Delta U)^2} = \frac{g'H}{(\Delta U)^2}, \quad \mathrm{Sc} = \frac{\nu}{\kappa_m}. \tag{3}$$

The Reynolds number, Re, compares advective to diffusive time scales for the flow. The bulk Richardson number, Ri_b, compares the potential energy of the flow to the shear-induced kinetic energy. The Schmidt number, Sc, compares the diffusivity of momentum to the mass diffusivity.

In a linear stability analysis, we expand our variables as

$$\mathbf{u}(\mathbf{x}, t) = (U(y, z), 0, 0) + \epsilon\check{\mathbf{u}}(\mathbf{x}, t), \quad |\epsilon| \ll 1, \tag{4a}$$

$$p(\mathbf{x}, t) = P(y, z) + \epsilon\check{p}(\mathbf{x}, t), \tag{4b}$$

$$\rho(\mathbf{x}, t) = \mathcal{R}(z) + \epsilon\check{\rho}(\mathbf{x}, t), \tag{4c}$$

where $\mathbf{x} = (x, y, z)$, i.e., as a sum of a steady base flow and arbitrarily small perturbations. The base flow is assumed parallel to the duct and invariant in the streamwise direction x. Expansions of Eqs. (4a) are then plugged into Eqs. (2a), leading to linear equations for the perturbations at $O(\epsilon)$. The x (and t) invariance of the base flow and infinite extent of the domain in x allow us to express any perturbation $\check{f}$ as Fourier modes in x and t:

$$\check{f} = \hat{f}(y, z)\exp(ikx + \sigma t) + \mathrm{c.c.} \tag{5}$$

Since we consider temporal instabilities in this paper, we set the wavenumber $k \in \mathbb{R}$ and $\sigma \in \mathbb{C}$, such that the real part of σ represents the growth rate while its imaginary part represents the frequency.

As explained in Ref. [12], the dimensionality of the system (number of flow variables) can be reduced at the cost of increasing its differential order. In this paper, keeping the primitive variable formulation ($\hat{u}, \hat{v}, \hat{w}, \hat{\rho}, \hat{p}$) would be preferred in order to avoid fourth-order derivatives that, with the discretization method presented later, would lead to poor matrix conditioning. However, this leads to problematic storage requirements. Consequently, we adopted the compromise proposed in Ref. [13]: $\hat{u}$ was eliminated, leading to at most third-order derivatives of $\hat{v}, \hat{w}$. Rewriting the continuity equation as $\hat{u} = ik^{-1}(\partial_y\hat{v} + \partial_z\hat{w})$ and plugging it into the x-momentum equation results in the following generalized eigenvalue problem (dropping the inverted hats):

$$\sigma\begin{bmatrix} \mathcal{I} & & & \\ & \mathcal{I} & & \\ & & \mathcal{I} & \\ \partial_y & \partial_z & & \end{bmatrix}\begin{bmatrix} v \\ w \\ \rho \\ p \end{bmatrix} = \begin{bmatrix} \mathcal{L}_v & & & \mathcal{L}_{vp} \\ & \mathcal{L}_w & \mathcal{L}_{\rho w} & \mathcal{L}_{wp} \\ & \mathcal{L}_{w\rho} & \mathcal{L}_\rho & \\ \mathcal{L}_{pv} & \mathcal{L}_{pw} & \mathcal{L}_{p\rho} & \mathcal{L}_{pp} \end{bmatrix}\begin{bmatrix} v \\ w \\ \rho \\ p \end{bmatrix}, \tag{6}$$

where

$$\mathcal{L}_v = -ikU + \mathrm{Re}^{-1}\Delta,$$

$$\mathcal{L}_{vp} = -\partial_y,$$

$$\mathcal{L}_w = -ikU + \mathrm{Re}^{-1}\Delta,$$

$$\mathcal{L}_{w\rho} = -\mathrm{Ri}_b\cos(\theta),$$

$$\mathcal{L}_{wp} = -\partial_z,$$

$$\mathcal{L}_{\rho w} = -\partial_z \mathcal{R},$$

$$\mathcal{L}_{\rho} = -ikU + (\mathrm{ScRe})^{-1}\Delta,$$

$$\mathcal{L}_{pv} = -ikU\partial_y + ik\partial_y U + \mathrm{Re}^{-1}(-k^2\partial_y + \partial_{yyy} + \partial_{zzy}),$$

$$\mathcal{L}_{pw} = -ikU\partial_z + ik\partial_z U + \mathrm{Re}^{-1}(-k^2\partial_z + \partial_{yyz} + \partial_{zzz}),$$

$$\mathcal{L}_{p\rho} = -ik\mathrm{Ri}_b \sin(\theta),$$

$$\mathcal{L}_{pp} = -k^2.$$

Note that Δ is the Laplacian operator in x Fourier space, $\Delta = (-k^2 + \partial_{zz} + \partial_{yy})$, and $\mathcal{I}$ is the identity operator.

The solid and impermeable duct walls were modeled by no-slip boundary conditions for velocities and no mass flux for the density:

$$v = w = \partial_y v = \partial_y \rho = 0 \quad \text{for} \quad y = \pm B, \quad \forall z, \tag{7a}$$

$$v = w = \partial_z w = \partial_z \rho = 0 \quad \text{for} \quad z = \pm 1, \quad \forall y, \tag{7b}$$

where the $\partial_y v = \partial_z w = 0$ conditions result from the continuity equation ($iku = -\partial_y v - \partial_z w = 0$ at the walls).

The equations were discretized by a custom-built two-dimensional Chebyshev pseudospectral method. Note that this method represents a nontrivial improvement in accuracy and speed upon the finite-difference method of Ref. [12]. More details on the discretization and the numerical solution are given in Appendix C.

3. Base flows

Our analytical base flows $U(y, z)$ and $\mathcal{R}(z)$ were chosen to be both simple and realistic. For the velocity we considered

$$U(y, z) = -\sin(\pi z)M(y) \quad \text{for} \ -1 \leqslant z \leqslant 1 \ \text{and} \ -B \leqslant y \leqslant B. \tag{8}$$

The spanwise modulation $M(y)$ can take one of the two following shapes:

$$M_p(y) = 1 - (y/B)^2, \tag{9a}$$

$$M_\gamma(y) = \frac{\tanh\left[\gamma(1 - (y/B)^2)\right]}{\tanh \gamma}. \tag{9b}$$

Figure 2 shows the profiles M_p, M_γ for the two different values of γ used in this paper. Both profiles satisfy no-slip conditions at the walls. The "Poiseuille" profile M_p represents a steady, fully developed boundary layer extending throughout the entire y domain from one wall to the other. The "tanh" profile M_γ has a parameter γ whose increase above 1 generates increasingly flat profiles in the midplane $y = 0$ and thin boundary layers at the walls. It models a flow whose spanwise boundary layer did not have sufficient time and/or length to develop fully. (The *local* stability analysis requires the Reynolds number (Re) to be sufficiently large such that streamwise variations are on larger scales than the instability wavelength in order to remain relevant.) A fully developed sine shape is used in z in all cases, as this paper focuses on the effect of spanwise confinement. As a comparison, the experimental mean flow of Ref. [12] also has roughly a sine shape in z (although slightly asymmetrically down-shifted), and our M_γ in y is an excellent approximation with a best fit obtained for $\gamma \approx 2.1$.

For the base density distribution, we considered the classical hyperbolic tangent $\mathcal{R}(z) = -\tanh[(z - z_0)/\delta]$. This introduces two additional degrees of freedom: the density layer thickness ($\sim 2\delta$) and the asymmetry (or shift) parameter z_0. The scaling of the sine profile, Eq. (8), sets the
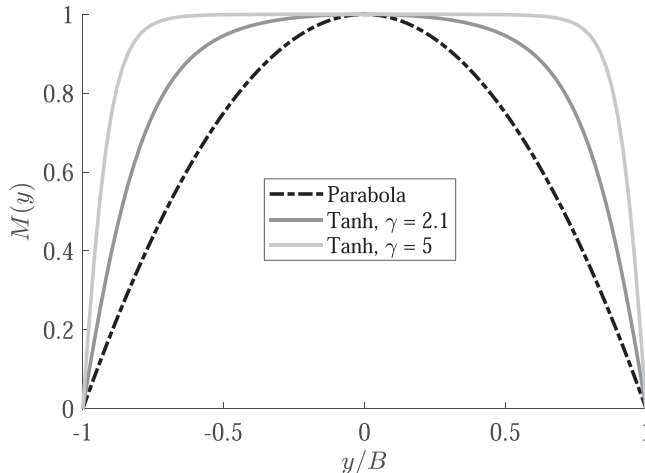
FIG. 2. Illustration of the three different spanwise profiles, $M(y) = M_p(y)$ (black dashed), $M_{2.1}(y)$ (dark gray solid), and $M_5(y)$ (light gray solid), used in the rest of the paper. The full base velocity is $U(y, z) = -\sin(\pi z)M(y)$.

shear layer thickness to 1, leading to

$$\mathcal{R}(z) = -\tanh\left[2R(z - z_0)\right] \quad \text{for } -1 \leqslant z \leqslant 1, \tag{10}$$

where we define $R = 1/(2\delta)$ as the ratio of the shear layer thickness to the density layer thickness.

4. Approach

We are left with eight free parameters: Re, Sc, Ri_b, θ, z_0, R, $M(y)$, and B. By choosing their values, and given a wavenumber $k \in \mathbb{R}^+$, all operators in Eq. (6) are made fully explicit: the generalized eigenvalue problem can be solved numerically for both $\sigma(k) \in \mathbb{C}$ and its associated eigenvector $[v, w, \rho, p]$. We express $\sigma(k) = \sigma_r(k) + i\sigma_i(k)$ where the subscripts r and i respectively denote the real part (growth rate) and the imaginary part. Therefore, here the phase velocity is $-\sigma_i(k)/k$ and the wave propagates in the positive x direction if it is positive. If $\sigma_r(k) > 0$ the wave is unstable and grows as $\propto e^{\sigma_r t}$ until nonlinearities come into play (see Ref. [14] for a treatment of these nonlinearities).

The eight free parameters are not all significant when focusing on the effect of spanwise confinement. The first key parameter for confinement is evidently the duct aspect ratio B. In addition, we investigate the impact of viscous effects on both the base flow, by varying $M(y)$ and γ, and also on the perturbation dynamics, by varying Re. As the base flow is not directly dependent on Re, both effects can be studied independently. Finally, in this paper, we also vary Ri_b, the central parameter for stratified shear instabilities. Therefore, in the remainder of the paper, the four remaining parameters will typically be set according to the experimental values of Ref. [12]: $(\text{Sc}, R, z_0, \theta) = (700, (1/0.047)/2, -0.22, 5°)$.

B. Summary of classical results (1D, unconfined)

Since our study focuses on the effects of spanwise confinement, comparison with a classical (one-dimensional, unconfined, and spanwise-invariant) analysis is appropriate. In this problem, which we refer to simply as the "1D problem," all y dependence is removed ($\partial_y = 0$) in Eq. (6), and the base flow is $U(z) = -\sin(\pi z)$. This leads to a simpler system, whose expression is given in Appendix A. Note that by "1D" we do *not* mean that the spanwise direction does not exist, but that

it is infinite and that no spanwise variations exist either for the base flow or the perturbations. This distinction should be kept in mind in the following.

As a foundation for our analysis of spanwise confinement, we now summarize the effects of the prominent parameters (Re, Ri_b) on the "1D" stability properties. This short discussion results from supplementary 1D computations, which for the sake of brevity are not illustrated. In addition, although fixed elsewhere, the effect of the parameter z_0 (quantifying the offset between the density and velocity base profiles) on the '1D stability properties is briefly presented as well.

Effects of Re. The growth rates σ_r increase monotonically and relatively uniformly with Re, until Re ≈ 1000, where this effect tends to saturate.

Effects of Ri_b. When the flow is unstratified, with $Ri_b = 0$, the flow is only subject to a "pure" Kelvin-Helmholtz (denoted KH) instability. As Ri_b increases, the KH mode is progressively weakened (i.e., σ_r decreases) and eventually suppressed ($\sigma_r = 0$), since, physically speaking, too much potential energy is required to allow the rolling up of the shear layer, and hence the density stratification. At $Ri_b \approx 0.125$ the flow then becomes subject to the inherently stratified Holmboe instability (denoted H), which is characterized at finite amplitude by propagating waves localized at the density interface ($z = z_0$), which generally counterpropagate. The growth rate of the Holmboe instability initially increases with Ri_b, up to a certain value, before σ_r starts decreasing again. The most unstable wavenumber k increases monotonically with Ri_b, since, in physical terms, longer waves require too much potential energy to allow instability. A physical mechanism based on wave interaction is now commonly proposed to explain the KH and H instabilities, as exhaustively reviewed in Ref. [15], although the underlying arguments date back to Taylor's Adams Prize essay in 1915. Using a broken-line profile model for the shear layer and a localized density jump, the KH instability can be interpreted as the interaction between the two counterpropagating vorticity waves localized at and "riding" their respective vorticity interfaces. In contrast, the H instability appears as an interaction between one of the two vorticity waves, with one of the two gravity waves, that both "ride" the density interface. Discrimination is then made by noticing that, in order to interact, a wave pair must have *intrinsic* phase speeds of opposed sign. This is shown in Ref. [15] as being equivalent to the Rayleigh theorem.

Effects of z_0. For $z_0 = 0$, the flow and the Holmboe instability are symmetric, in the sense that the distances between both vorticity waves and the density interface are equal. Both Holmboe waves are thus equally unstable and propagate with equal and opposite phase speeds. Mathematically, the corresponding eigenvalues are complex conjugates of each other. When $z_0 < 0$, this symmetry is broken; the left-going wave ("H_l") becomes slower, of longer wavelength, and more unstable, while the right-going wave ("H_r") becomes faster, of shorter wavelength, and more weakly unstable (and vice versa, there is a perfect symmetry in the case $z_0 > 0$ by swapping H_r and H_l).

III. MOST UNSTABLE MODE: PRELIMINARY OBSERVATIONS

We now solve numerically the fully 2D generalized eigenvalue problem, Eq. (6), with confinement in both the crosswise and spanwise directions. We choose a Poiseuille spanwise profile $M(y) = M_p(y)$, and parameters (Re, Sc, R, z_0, θ) = $(440, 700, (1/0.047)/2, -0.22, 5°)$ (as in Ref. [12]), and three different aspect ratios $B = [1, 3, 5]$. The corresponding 1D (spanwise-invariant) problem is also solved for comparison (it can be viewed as the limit $B \to \infty$). It is not clear at this stage whether this 1D mode will be more unstable than 2D modes, since the duct walls create transverse shear in their vicinity (i.e., crosswise vorticity $\omega_z = \partial_y U$), whose effect is, as yet, unknown.

The dispersion relations of the *most unstable* mode of the 2D spectrum are plotted with solid lines for $k = [0, 4.5]$ in Fig. 3 for various B and Ri_b. For comparison, the 1D case (with $B \to \infty$) is plotted with a dot-dashed line. Note that the most unstable mode (shown here with solid lines) has no reason to be the *only* unstable mode for a given k. In Fig. 3(a), the second most unstable unstratified mode is plotted with a dashed line for comparison for the case $B = 1$. Furthermore, in the 1D stratified problem, we generally have two unstable H modes, easily distinguishable by the sign of the phase speed. In the 2D problem, as B increases, we also find an increasing number of
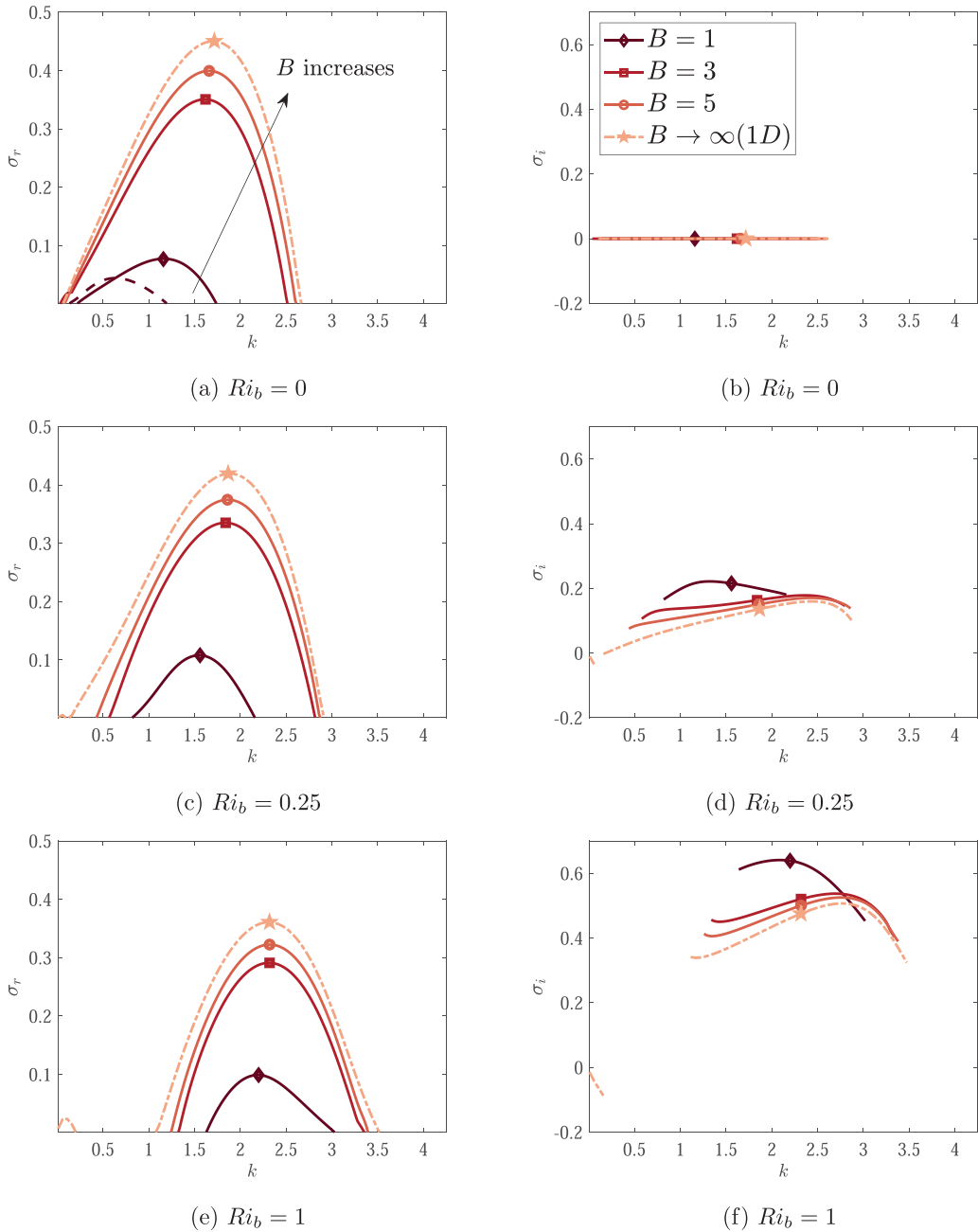
FIG. 3. Dispersion relations of the most unstable mode of the spectrum. The left column shows the growth rate σ_r, and the right column shows the frequency σ_i. We chose a Poiseuille spanwise profile M_p, four different aspect ratios B, and three different Ri_b (rows). Solid and dashed lines stand for the 2D problem and the lighter shade of grey corresponds to higher B in the set $B = [1, 3, 5]$. Dash-dotted lines mark the 1D problem ($B \rightarrow \infty$). A marker, which is different for each B, indicates the maximum growth rate ($k = k_m$).

unstable modes with similar phase speeds; however, we defer this analysis to Sec. IV in order to first focus on the most unstable mode here.

A. Kelvin-Helmholtz to Holmboe transition

Figure 3 shows the following transitions between KH and H modes:

(i) At $Ri_b = 0$ [Figs. 3(a) and 3(b)], the solid lines correspond to a KH mode, while the dashed line (second most unstable mode) corresponds to a fully 3D mode, which exists at $B = 1$ and peaks at $k \approx 0.6$. To the authors' knowledge, this mode of instability is yet unclassified, and its characterization is deferred to Sec. V. Both the KH mode and this fully 3D mode have zero phase speed.

(ii) At $Ri_b = 0.25$ [Figs. 3(c) and 3(d)], the dispersion relation corresponds to an H_l mode (Holmboe traveling left). As shown in Ref. [10], the frontier between KH and H modes at intermediate Ri_b is blurred as soon as $z_0 \neq 0$, but we believe that $Ri_b = 0.25$ is sufficiently large for Holmboe modes to dominate unambiguously. As we choose a relatively strong negative asymmetry $z_0 = -0.22$, the H_r mode (traveling right) is absent (i.e., stable), just as in the 1D problem.

(iii) At $Ri_b = 1$ [Figs. 3(e) and 3(f)], the previous H_l mode remains. We also note the barely visible existence of a very weakly unstable 1D mode for $k \approx 0-0.2$ [also barely visible in Fig. 3(c)], related to the nonzero tilting angle effect $\theta \neq 0$, the analysis of which is beyond the scope of this paper.

We now discuss the effect of spanwise confinement on the dispersion relations. In the present temporal stability analysis ($k \in \mathbb{R}$ and $\sigma \in \mathbb{C}$), both KH and H modes are stabilized by the spanwise confinement: values of σ_r monotonically decrease below their 1D upper bounds for all wavenumbers k as B decreases. This stabilizing effect is more pronounced at small B. In this process, the most unstable wavenumber k_m is approximately conserved, or perhaps very slightly decreased.

Note that the stabilizing effect of the sidewalls is in accordance with the results shown in Refs. [16–18]. These three studies establish the linear stability of an unstratified pressure-driven flow through a rectangular duct, namely, a two-dimensional equivalent to the canonical plane Poiseuille flow. The analytical work Ref. [16] considers the wide aspect ratio $B \gg 1$ limit, and performs a multiple asymptotic expansion based on the small parameter B^{-1}. In this asymptotic regime, a decrease in B leads to an increase in the critical Reynolds number from the one-dimensional prediction $Re_{cr} = 5772.22$. This conclusion is qualitatively supported by the numerically oriented work [17,18], that does not assume any particular regime for B. Physically, this stabilization was attributed in Ref. [16] to a finite-Re effect, more precisely to the presence of spanwise boundary curvature in the base flow introduced by the sidewalls. Such physical interpretation remains to be verified in our case, as now attempted in Sec. III C.

B. Convective to absolute instability transition

Our temporal stability analysis has implications on the spatiotemporal properties of these flows. With increasing confinement (decreasing B), longer waves (traveling left) are sped up, evidenced by the σ_i curves being shifted up at low k in Figs. 3(b), 3(d), and 3(f). The shortest waves, on the other hand, are slowed down, presumably because they encounter more significant viscous effects. An interesting consequence of this selective speed up and slow down is that the group velocity of the unstable wave-packet centroid, defined as

$$V_m = -\frac{d\sigma_i}{dk}(k_m),$$

flips its sign as B is reduced from ∞ to 0. This means that there exists a value of B such that the wave-packet centroid is static.

For example at $Ri_b = 0.25$ [Fig. 3(d)], the slope at the marker $d\sigma_i/dk(k_m)$ vanishes somewhere between $B = 3$ and $B = 1$. In the meantime, it is clear in Fig. 3(c) that the flow remains unstable. This implies that, for the chosen set of parameters, confinement effectively renders the flow
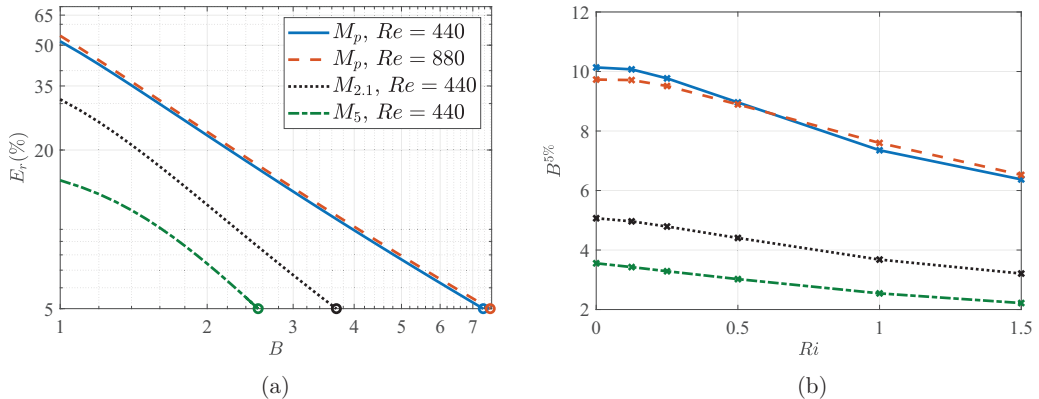
FIG. 4. Stabilizing effects of the aspect ratio B, spanwise profile $M(y)$, and Re. (a) Relative error between the 1D and 2D most unstable growth rate evaluated at the most unstable 1D wavenumber $k_m^{1D} \approx 1.88$. Three different spanwise profiles and two different Re are chosen, all for $\mathrm{Ri}_b = 1$. A circle symbol is placed at the threshold aspect ratio $B^{5\%}$ where the error is $E_r = 5\%$; (b) variation of this threshold aspect ratio $B^{5\%}$ with Ri_b.

absolutely unstable, since an unstable wave packet centered in $V_m = 0$ necessarily corresponds to an absolute instability. For $\mathrm{Ri}_b = 0.25$, where the derivative is always of a small amplitude, the H_l wave is very likely to be absolute for all the B shown. However, for $\mathrm{Ri}_b = 1$, it may be convective for $B = 5$, whereas it is certainly absolute for some $B \in [1, 3]$. In this latter case, we conclude that spanwise confinement would *destabilize* the flow in a spatiotemporal sense. A rigorous saddle-point [19–23] or impulse response [24–27] approach would be interesting in future work as discussed further in Sec. VI.

C. Stabilization by sidewalls and base flows

We previously attributed the stabilizing influence of confinement to a finite-Re effect. To investigate this further, we analyze separately the effects of viscosity on (i) the base flow and (ii) the perturbations. For case (i) we keep $\mathrm{Re} = 440$ but switch the spanwise profile from $M_p(y)$ to $M_{2.1}(y)$ and $M_5(y)$ (decreasing the boundary layer thickness; see Fig. 2). For case (ii) we keep $M(y) = M_p(y)$ but double Re to $\mathrm{Re} = 880$.

To quantify the (temporally) stabilizing effect of spanwise confinement, we define E_r as the relative difference between the 1D most unstable eigenvalue $\sigma_m^{1D} = \sigma^{1D}(k_m^{1D})$ and the 2D eigenvalue evaluated at the same (1D most unstable) wavenumber $\sigma(k_m^{1D})$:

$$E_r(B) = \frac{\left\| \sigma_m^{1D} - \sigma\left(k_m^{1D}; B\right) \right\|}{\left\| \sigma_m^{1D} \right\|}.$$

Choosing $\sigma(k_m^{1D})$ instead of σ_m allows us to avoid solving the 2D eigenvalue problem for several k at each B (in order to find k_m). In addition, we are interested in the limit $B \to \infty$ where it is clear in Figs. 3(a), 3(c), and 3(e) that k_m^{1D} becomes an excellent approximation of the 2D most unstable wavenumber k_m for $B \gg 1$ (already for $B = 3$, and even more so at the strong stratification $\mathrm{Ri}_b = 1$).

In Fig. 4(a) we therefore plot $E_r(B)$ (in percentage terms) in the four cases considered, setting $\mathrm{Ri}_b = 1$. Only differences greater than $E_r \geqslant 5\%$ are shown since lower values required computationally prohibitive B values. First, we see that, for a given $\mathrm{Re} = 440$, difference curves for the tanh profiles M_γ are significantly lower than for the Poiseuille profile M_p, and even more so for larger values of γ. In other words, base flows with thinner boundary layers yield growth rates σ_r that are less affected (in the specific sense of being less stabilized) by sidewall confinement. Interpreting the 1D problem as an unbounded and constant $M(y) = 1$, it appears natural indeed

to expect convergence of σ for a base flow that resembles $M(y) = 1$ over the longest y interval, which is here $M_5(y)$ (followed by $M_{2.1}$, and finally M_p). Interestingly, this also suggests that in these stratified shear instabilities, the spanwise boundary layers have a pure stabilizing effect. In broad terms, the boundary layer structure simply decreases the amount of kinetic energy available from the base flow to feed the instability, without introducing a viscous instability mechanism (e.g., Tollmien-Schlichting waves), at least at the values of Re considered therein.

Second, we observe in Fig. 4(a) that both dash-dotted lines for Re $= 440$ and 880 almost collapse on each other. That indicates that, when viscous diffusion affects the perturbation *alone*, its impact on the convergence towards the 1D problem is very weak. We conclude that if viscous effects have indeed generally a strong damping impact on stability properties, it is most significantly through their indirect effect on the base flow rather than through their direct effect on the perturbations dynamics alone.

We are now interested to know if the previous observations remain true for other values of Ri_b. Therefore in Fig. 4(b), we focus on the evolution with Ri_b of the threshold aspect ratio $B^{5\%}$, for which the error is $E_r(B^{5\%}) = 5\%$ [highlighted by a circle on the x axis of Fig. 4(a), where we set $Ri_b = 1$]. We see that our conclusions for $Ri_b = 1$ remain valid for other values of $Ri_b \in [0, 1.5]$. We further learn from Fig. 4(b) that this threshold aspect ratio is reduced with increasing stratification: the pure KH mode at $Ri_b = 0$ is the most affected by the stabilizing influence of boundary layers, whereas the H mode at high Ri_b appears to easily match its 1D counterpart; i.e., it is least affected by confinement. This might be linked to the fact that higher Ri_b are linked to shorter wavelengths which naturally tend to be less affected by the relatively more distant walls. In the next section we will see that confinement heavily affects Holmboe modes in more subtle ways, through the creation of spanwise harmonics.

IV. SPANWISE HARMONIC HOLMBOE MODES

A. Eigenvalue spectra and oblique mode analysis

Heretofore, given a wavenumber k, only the most unstable mode of the eigenvalue spectrum was represented in Fig. 3 (and used in Fig. 4). Whereas this mode is unique in the 1D problem as a consequence of the strong asymmetry (quantified by z_0) that stabilizes the opposite Holmboe wave, it has no reason to be in the 2D problem. In fact, there exists a fairly important number of unstable modes besides the most unstable one; they are now shown in Fig. 5. In the left column, we show the unstable part of the spectrum (black squares) for a Poiseuille spanwise base flow [Re $= 440$, $Ri_b = 0.25$, and $B = 3, 5$ corresponding to Figs. 3(c) and 3(d)]. In the right column, we replace $M_p(y)$ by $M_5(y)$. The 1D eigenvalue is systematically plotted (with black stars) for comparison. To understand the existence of these multiple unstable modes, we consider and superimpose (shown with a red curve) the dispersion relation of oblique modes, found by taking a spanwise independent flow $U(z) = -\sin(\pi z)$ [in other words, $M(y) = 1$], and expanding any perturbations field f, as

$$\hat{f}(y, z) = \overline{f}(z) \exp(i\beta y), \tag{11}$$

where $\beta \in \mathbb{R}$ is the spanwise wavenumber. A single mode (corresponding to a choice of k, β) is a propagating wave whose front is perpendicular to $(k\hat{\mathbf{x}} + \beta\hat{\mathbf{y}})$. It is clear that the eigenvalues $\sigma_r + i\sigma_i$ are now also functions of β. As $\beta \in \mathbb{R}$, all wavelengths are allowed for the perturbations, so that this description implicitly assumes that the spanwise direction is unbounded. It also requires the coefficients of the equations to be independent on y, so we must have, as introduced earlier, a spanwise-invariant base flow, i.e., $M(y) = 1$. This problem is therefore similar to the 1D one, except that perturbations are allowed to vary in y. In the rest of the paper, this problem will thus be referred to as the 1D-O problem ("O" for oblique). It is not *a priori* clear whether the $\beta = 0$ (i.e., the 1D) eigenvalue is the most unstable one among all possible β. A stratified generalization of Squire's theorem [28], presented in Ref. [29], states that a 1D-O mode ($\beta \neq 0$) has a smaller growth rate σ_r than a corresponding 1D mode ($\beta = 0$) having lower Re and a larger Ri_b. However, since H modes generally have σ_r increasing with Ri_b, this theorem is inconclusive in the present context and
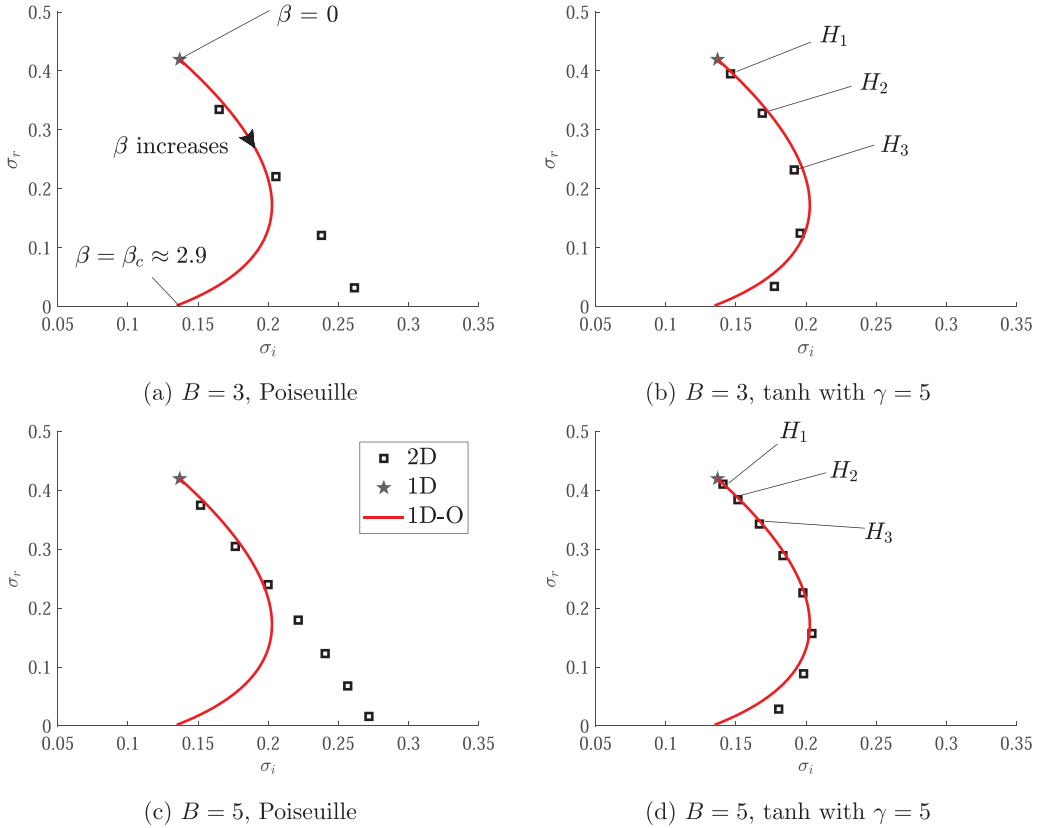
FIG. 5. Unstable part of the spectra for Re = 440, $\mathrm{Ri}_b = 0.25$, and $k = k_m^{1D} = 1.88$. We show two different aspect ratio flows $B = 3$, 5 and two different $M = M_p$, M_5. The black star symbol marks the 1D eigenvalue, the black squares are the 2D eigenvalues, and the red line is the 1D-O dispersion relation as a function of the spanwise wavenumber β. The latter is the same for the four panels as it does not consider the spanwise variations of the base flow. As a consequence of the strongly negative z_0, note that all eigenvalues are in the $\sigma_i > 0$ half plane.

does not preclude the dominance of 1D-O modes over 1D modes (for more details see Sec. 2.3.3 of Ref. [12]).

Let us now observe the 2D, 1D-O, and 1D unstable spectra, focusing first on the left column of Fig. 5 ($M = M_p$). At $B = 3$ [Fig. 5(a)], four 2D eigenvalues are unstable. As the aspect ratio is increased to $B = 5$ [Fig. 5(c)], these eigenvalues approach the 1D value and three new distinct unstable 2D eigenvalues appear by crossing the real axis, bringing the total to seven eigenvalues "originating" from the 1D eigenvalue. As a matter of fact, the 1D eigenvalue is always more unstable than the 2D ones. Oblique modes (red line) of course match the 1D eigenvalue for $\beta = 0$; as β increases, they draw a "comma" shape in the complex plane down to a cutoff $\beta = \beta_c$ where they cross the real axis and become stable. Note that the 1D-O eigenvalues, just as the 2D eigenvalues, never become more unstable than the 1D eigenvalue: the instability does not take "advantage" of the wave-front rotation, as it does for instance in Tollmien-Schlichting instability [30]. Oblique modes, and their associated spanwise curvature, simply undergo stronger viscous damping as β is increased. Indeed, the Laplacian term $\mathrm{Re}^{-1}(-k^2 + \partial_{zz} + \partial_{yy})$ becomes $\mathrm{Re}^{-1}(-k^2 + \partial_{zz} - \beta^2)$ under the oblique mode expansion (see Appendix B); thus, larger β give more weight to this diffusive term. Consequently, β_c is primarily determined by the value of Re; for the parameters of Fig. 5, we obtain $\beta_c \approx 2.9$.
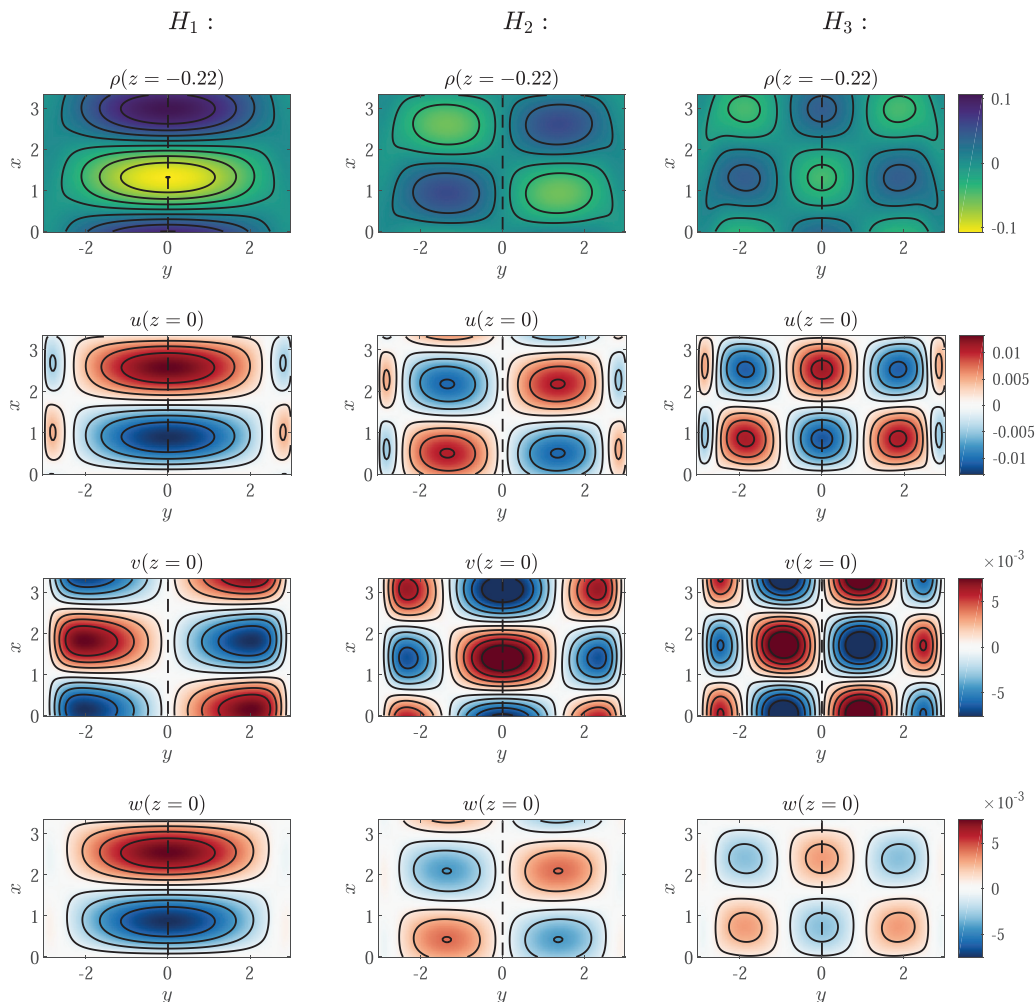
FIG. 6. Sliced views of ρ, u, v, w in the x-y plane of the three most unstable 2D eigenmodes of Fig. 5(b) (H_1, H_2, and H_3, from left to right, ordered by decreasing growth rates). The spanwise profile is $M(y) = M_5(y)$, and the parameters are Re $= 440$, Ri$_b = 0.25$, $B = 3$, $k = k_m^{1D} = 1.88$.

Focusing now on the right column of Fig. 5 ($M = M_5$), we observe exactly the same process as B is increased, except that 2D unstable modes become more numerous [five in Fig. 5(b) vs four in Fig. 5(a), and eight in Fig. 5(d) vs seven in Fig. 5(c)], and more tightly packed around the 1D one. More interestingly, however, the 2D eigenvalues fit much better the oblique mode dispersion relation, in particular at $B = 5$ [Fig. 5(d)], where the black squares appear to be nothing else than a discretized version of the red curve, with only a slight error for the more stable modes.

Note that an emergence from the 1D eigenvalue of an increasing number of inherently 2D eigenvalues as the aspect ratio is varied was already observed in Ref. [18] for Poiseuille flow. However, to the authors' knowledge, a quantitative comparison with the oblique dispersion relation is novel.
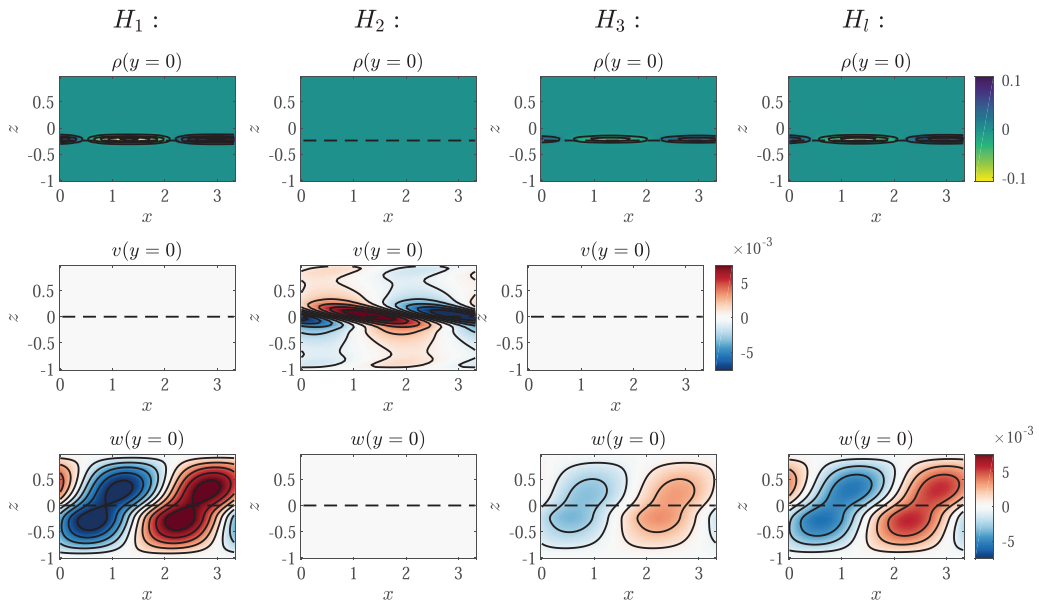
FIG. 7. Sliced view on the *x-z* plane of the three 2D most unstable eigenmodes for $k = k_m^{1D} = 1.88$. The 1D most unstable mode is added at the fourth column. Modes from left to right between the first and the third columns are H_1, H_2, and H_3, as ordered in decreasing order of growth rates. $M(y) = M_5(y)$, Re = 440, $Ri_b = 0.25$, and $B = 3$.

B. Spatial structures and symmetries

To understand this phenomenon better, we show in Fig. 6 the spatial structure of the three most unstable eigenmodes of Fig. 5(b), labeled H_1, H_2, and H_3, by decreasing growth rates. Each column shows an *x-y* slice of the eigenmode (in the plane $z = 0$ for velocities, and $z = z_0$ for the density). Although insufficient for a phenomenological understanding of the instability, this visualization allows us to compare the spanwise structure of eigenmodes with each other.

Two different types of *spanwise* symmetries are revealed. The first symmetry, that we call S_1, can be characterized as (even, odd, even, even) for (u, v, w, ρ), respectively. Namely, the field $u(y, z)$ is even around the axis $y = 0$, such that $u(-y, z) = u(y, z)$; meanwhile, the field $v(y, z)$ is odd around the axis $y = 0$, such that $v(-y, z) = -v(y, z)$, etc. The second symmetry, S_2, is its opposite: (odd, even, odd, odd). In both cases, v has a different symmetry from all other perturbation components. It can be checked that these two symmetries are indeed allowed by Eq. (6) as long as both U and $\mathcal{R}$ are even in y. We complete Fig. 6 with Fig. 7, showing *x-z* slices of the same three modes in the orthogonal plane $y = 0$. In the last column, we add the 1D mode H_l for comparison. Simultaneous observation of Figs. 6 and 7 allow us to draw the following conclusions.

(1) The most unstable 2D mode, H_1, has symmetry S_1. It appears to be a simple "2D extension" of the 1D mode for ρ, u, and w. Indeed, its *x-z* structure at $y = 0$ is extremely similar to the 1D structure, and we remember that symmetry S_1 guarantees that $v = 0$ everywhere on this plane (as in the 1D case). In addition, no particular spanwise variation is observed for ρ, u, and w (Fig. 6) other than those required to match the boundary conditions at the walls. This mode should be essentially seen as a two-dimensional version of H_l, and is identical to the confined Holmboe instability of Ref. [12].

(2) The second most unstable eigenmode H_2 has symmetry S_2, of which no 1D equivalent exists (compare the second and fourth columns of Fig. 7). The density interface is now also wavy in the spanwise direction. Structurally, this H_2 mode should be seen as a 'harmonic in *y*" of the first mode H_1. Indeed u, w, ρ have a spanwise "periodicity" of $2B$ (the quotes indicate that a true
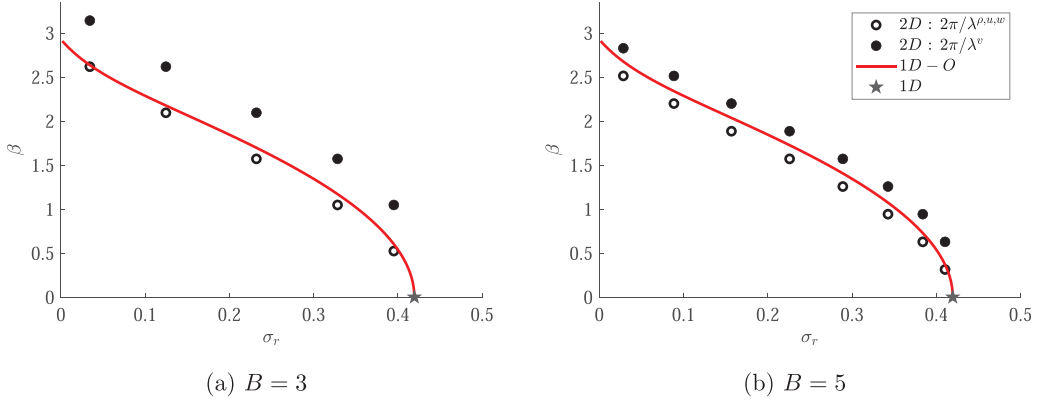
FIG. 8. Growth rates of oblique modes as a function of β (red line), and of 2D modes at $k = k_m^{1D} = 1.88$ as a function of *both* $\lambda_i^{\rho,u,w}$ (open circles) and λ_i^v (solid circles). Parameters are $M(y) = M_5(y)$, Re $= 440$, and Ri$_b = 0.25$. The 1D-O dispersion relation in β predicts the discrete 2D spanwise harmonics increasingly well as B is increased and $M_5(y) \to 1$ over most of the domain.

periodicity clearly cannot be satisfied because of the boundary conditions), in comparison to $4B$ in H_1; furthermore, v is now $(4B/3)$ periodic compared to being $(2B)$ periodic in H_1.

(3) The third most unstable eigenmode H_3 goes back to symmetry S_1, and is one step further in the harmonic range. The spanwise periodicity is now $(4B/3)$ for u, w, ρ and is B for v.

This emerging logic of alternating symmetries, as a consequence of higher-order harmonics, extends to higher modes: the fourth most unstable mode H_4 has symmetry S_2, the fifth has symmetry S_1, etc. Overall, if we rank modes by decreasing order of growth rate, then the ith mode, H_i, is S_1 if i odd and S_2 if i even. Spanwise "wavelengths" (the quotes again draw attention to the fact that the shape is not purely sinusoidal) are summarized as

$$\lambda_i^\rho = \lambda_i^u = \lambda_i^w = \frac{4B}{i} \quad \text{for } i = 1, 2, 3, \tag{12a}$$

$$\lambda_i^v = \frac{4B}{i+1} \quad \text{for } i = 1, 2, 3, \ldots. \tag{12b}$$

It is important to note that this mode structural ordering is conserved as we change B. Because of this "spanwise-periodic" shape of 2D modes, we now understand the (imperfect) alignment of corresponding eigenvalues on the oblique modes dispersion relation observed in Fig. 5(b) (and other panels). This may appear surprising since 2D modes propagate purely along x, whereas oblique modes make an angle β with the background flow. However, it is shown in Appendix B that modes that are periodic standing waves in y and that travel purely along the streamwise x direction satisfy the 1D-O dispersion relation (thanks to the symmetry of the system). These modes are

$$\begin{cases} \hat{h}(y,z) = \check{h}(z)\cos(\beta y) \\ \hat{v}(y,z) = \check{v}(z)\sin(\beta y) \end{cases} \text{ with symmetry } S_1, \quad \text{and} \quad \begin{cases} \hat{h}(y,z) = \check{h}(z)\sin(\beta y) \\ \hat{v}(y,z) = \check{v}(z)\cos(\beta y) \end{cases} \text{ with symmetry } S_2,$$

where h denotes u, w, ρ, or p [the hat and the breve are simply added to distinguish these particular mode shapes from the one arising directly from Eq. (6)]. Of course, the 2D eigenvalue spectrum necessarily remains a *discrete* version of this 1D-O dispersion relation (continuous in β) since only a few "wavelengths" satisfy the boundary conditions due to quantization.

To illustrate this point, we plot in Fig. 8 the wavelengths $\lambda_i^{\rho,u,w}$ and λ_i^v of the 2D modes together with the one predicted by the 1D-O dispersion relation, as a function of the growth rate (β vs σ_r plot). For $B = 3$ [Fig. 8(a)] the agreement between 2D and 1D-O "wavelengths" is very good, simply because 2D modes possess structures akin to 1D-O standing waves in y. The slight discrepancy

between 2D and 1D-O growth rates, previously observed in Fig. 5(b), may now be explained as follows. In the 1D-O problem, only one wavelength $\lambda = 2\pi/\beta$ is predicted for a given σ_r, and it is equal for all fields u, v, w, ρ. By contrast, in the 2D problem, we already reported that $\lambda_i^v < \lambda_i^{\rho,u,w}$. This mismatch is an interesting consequence of the system symmetry, to which is added the no-slip boundary conditions at $\pm B$. To be more specific, let us first focus on H_1 (the most unstable mode in Fig. 6). The corresponding 1D-O mode would predict a v that is phase shifted by $\pi/2$ in y with respect to all the others fields; thus, $|v|$ would be zero in the middle of the duct and maximum at $y = \pm B$, violating the no-slip boundary conditions. Therefore, the 2D mode adapts by decreasing its wavelength by the least possible amount so that the right and left lobes of v cancel at the walls. A similar phenomenon happens in all the other unstable modes. The 2D growth rate is then determined by a compromise between both wavelengths. Consequently, reversing the paradigm and fixing a value of σ_r in Fig. 8, we can say that the 1D-O wavelength is above λ_i^v and below $\lambda_i^{\rho,u,w}$.

Last but not least, oblique modes require a y-invariant base flow $M(y) = 1$ whereas the tanh 2D base flows have boundary layers near the wall. This additional source of discrepancy between 2D and 1D-O modes is clearly illustrated by comparing Fig. 5(c) ($B = 3$) to Fig. 5(d) ($B = 5$): the alignment of 2D eigenvalues on the 1D-O dispersion relation is clearly improved, and becomes very good, by reducing the relative boundary layer thickness. Moreover, increasing B improves the alignment and makes the 1D-O model increasingly accurate. Indeed, the difference between the u, w, ρ, and v wavelengths tends to zero as B increases, since

$$\frac{1}{\lambda_i^v} - \frac{1}{\lambda_i^{\rho,u,w}} = \frac{1}{4B}. \tag{13}$$

Since this difference is caused by the nonmatching of boundary conditions of v at the walls, it is logically attenuated as they are moved away. We indeed see that solid and open circles are closer to each other in Fig. 5(d) [compared with Fig. 5(b)], and in Fig. 8(b) [compared with Fig. 8(a)].

C. Importance of spanwise harmonics at weak confinement ($B \to \infty$)

We now address the question of higher harmonics becoming unstable, and/or even more unstable, as B is increased. Considering Eq. (12a), the answer comes naturally: the "wavelength" of the ith mode increases with B. Physically, the mode is stretching out as the walls are moved away. Consequently, the "wavenumber" $\beta_i^{2D} = 2\pi/\lambda_i^v$ or $2\pi/\lambda_i^{\rho,u,w}$ decreases, but we saw with the 1D-O analysis [Figs. 8(a) or 8(b)] that lower β corresponds to higher σ_r since such modes experience less viscous damping. In the limit $B \to \infty$, we expect the number of unstable modes to be infinite since $\Delta\beta_i^{2D} \propto B^{-1} \to 0$: we can have an infinite number of i before reaching the viscous cutoff β_c. In other words, in this limit, the discrete set of 2D unstable eigenvalues becomes a continuous spectrum, as one should expect from a Fourier *transform* in an infinite domain, as opposed to a Fourier *series* in a bounded domain. Moreover, in this limit, the 2D unstable spectrum is expected to *become* the 1D-O one if we choose $M(y) = 1$.

The above comments, although generally expected and relatively unsurprising, may have interesting implications for linear stability analyses at large aspect ratios $B \to \infty$. Namely, provided the base flow is almost y invariant far from the boundaries and has no v velocity, we conclude the following:

(1) The set of 1D-O eigenvalues for $\beta = \frac{2\pi i}{4B}$ with $i \in \mathbb{Z}$ gives an excellent prediction of the 2D spectrum.

(ii) The 2D spectrum becomes increasingly denser; 2D unstable eigenvalues are numerous, and the most unstable ones are very close, even though they correspond to modes with different spatial structures. As a practical consequence, if a given spanwise eigenmode is preferentially excited (for whatever reason), one may observe a pattern that is completely different from that predicted by the 1D analysis.

V. "TWISTED KELVIN-HELMHOLTZ" MODE

A. Dominance of a new mode KH_T at low k and $Ri_b \approx 0$

For particular combinations of Ri_b, k, and B (everything else being held fixed), it may occur that one of the previously described simple "2D extensions" of a 1D mode is not the dominant one. The dashed lines in Fig. 3(a) ($Ri_b = 0$) show that it can indeed happen. This phenomenon actually appears inherently unstratified, and quickly disappears as Ri_b increases. This "new" mode, briefly mentioned in Sec. III, will be referred to as KH_T in the following, since is actually a "twisted" version (with dominant crosswise vorticity) of KH_1, itself the 2D generalization of a "classical" 1D KH mode. Indeed, the eigenmode KH_T is shown in Figs. 9 and 10, where the most unstable mode for $B = 1$ is chosen. In particular, Fig. 9 shows a qualitative 3D visualization of the associated perturbation velocity streamlines, together with two equal and opposite isocontours of the corresponding crosswise vorticity ω_z. For comparison, Fig. 9(a) shows a similar visualization of KH_1, but with the "twisted" (i.e., rotated by a quarter turn) crosswise vorticity replaced by the (classical) spanwise vorticity ω_y of a KH mode.

The structure of KH_T is composed of alternated counter-rotating vortices, contained in the region $-0.5 \leqslant z \leqslant 0.5$. Streamlines are looping primarily in x-y planes, although they are slightly inclined along x. In other words, the perturbation vorticity is "twisted" so that it is primarily directed along z, with a slight component along x. This contrasts with KH_1 (or H_1), where the perturbation vorticity is primarily along y, which corresponds to the familiar "billow" vortices in x-z planes in Fig. 9(a).

Figure 10 shows a more quantitative visualization of the KH_T structure, with sliced view of ω_z and velocities on three orthogonal planes ($y = 0$, $z = 0$, $x = 7.3$, respectively, in the left, middle, and right columns). From the first column of Fig. 10, it appears that isocontours of $\omega_z(y = 0)$ are fully contained in the region $-0.5 \leqslant z \leqslant 0.5$, where $\partial_z U \leqslant 0$. Moreover, $\omega_z(y = 0)$ reaches a maximum amplitude exactly at $z = 0$, just as $\partial_z U(y = 0) = \pi \cos(\pi z)$ does. Unsurprisingly, this corresponds to the x location where $v(y = 0) = 0$, i.e., the center of the vortex. From the view of $\omega_z(z = 0)$ in the x-y plane, we learn that these vortices are associated with strong values of $\omega_z(z = 0)$ of opposite sign near the sidewalls. This is a consequence of the no-slip boundary conditions, which also induce a strong viscous dissipation. The main vortices are slightly positively sloped along x, and we observe a weak but nonzero value of $w(z = 0)$ perfectly in phase with $u(z = 0)$.

As we see in Figs. 9 and 10, contrary to the stratified case in Fig. 6, KH_T is *not* a harmonic of KH_1 in the sense that the wavelength of v of the former has decreased with respect to the one of the latter. Because the density interface does not exist at $Ri_b = 0$, the spanwise velocity has no need to adapt to the increase in the wavelength of the density perturbation. In turn, the quantization proposed in Eq. (12b) does not hold in this unstratified case, or indeed even in related relatively weakly stratified cases. This wavelength decrease in v, although not in u or in w, implies that KH_T may even become more unstable than KH_1 itself in weakly stratified situations.

The growth rates of KH_1 and KH_T are compared in the (k, B) plane in Fig. 11 (for $Re = 440$, $Ri_b = 0$). The left and right columns show the growth rates of KH_1 and KH_T, respectively. In addition, we investigate the effect of $M(y)$ on the stability properties of KH_T: the first row shows $M(y) = M_5(y)$ while the second row shows $M(y) = M_p(y)$. The red line is the locus where the growth rates of KH_1 and KH_T are equal; on its left, in the gray shaded area, KH_T is indeed more unstable than KH_1. The black line is the most unstable growth rate $\sigma_m(B)$ over k, and shows that for a given aspect ratio B, the most unstable mode is always KH_1 (the red curve never crosses the black curve), as expected. However, there is a low-k range starting from $k = 0$ where KH_T locally dominates. Interestingly, the width of this range has a nonmonotonic evolution: it reaches a maximum for $B \approx 1$ for the Poiseuille base flow and $B \approx 1.5$ for the tanh base flow. Increasing B above this value quickly reduces the region of dominance of KH_T. In other words, two effects compete as B decreases:

(1) The first effect is that KH_T "takes advantage" of confinement more than KH_1. Comparing Figs. 11(c) and 11(d), we see that as B decreases, KH_T has a region below $B \approx 1.75$ where σ_r increases again. This leads to the creation of an "island" in the σ_r contours centered around $B \approx 1.4$
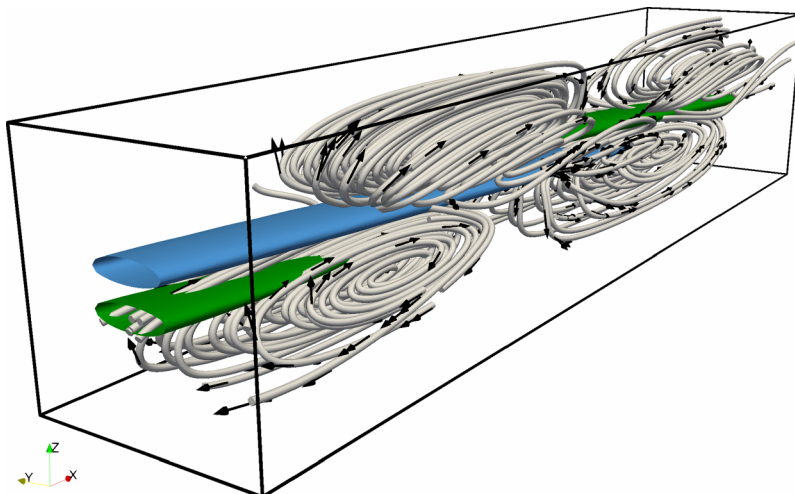
(a)
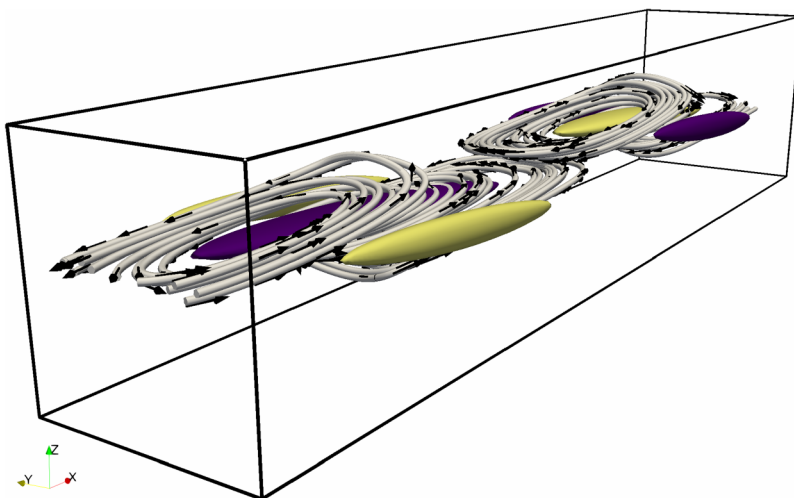
(b)

FIG. 9. Visualizations of the KH_1 and KH_T eigenmodes for $B = 1$ and $k = 0.64$ where $\sigma_r(k = 0.64) \approx$ 0.0440, ($M = M_p(y)$, Re = 440, Ri$_b$ = 0), highlighting their different spatial structure. (a) KH_1, where blue and green surfaces are isocontours of equal and opposite values of ω_y; (b) KH_T, where yellow and magenta surfaces are isocontours of equal and opposite values of ω_z

and $k \approx 0.5$. In the meantime, KH_1 is monotonically damped, and it is precisely this divergence in the behavior of both instabilities that leads to the enlargement of the gray shaded region where KH_T dominates. The tanh profile case behaves in a similar fashion, although the span of the KH_T-dominated region is reduced for intermediate values of B. This suggests that KH_T can take advantage of the spanwise confinement only if the induced crosswise vorticity is located at the center of the duct (rather than at the walls), at least as long as there is enough vorticity at the center.
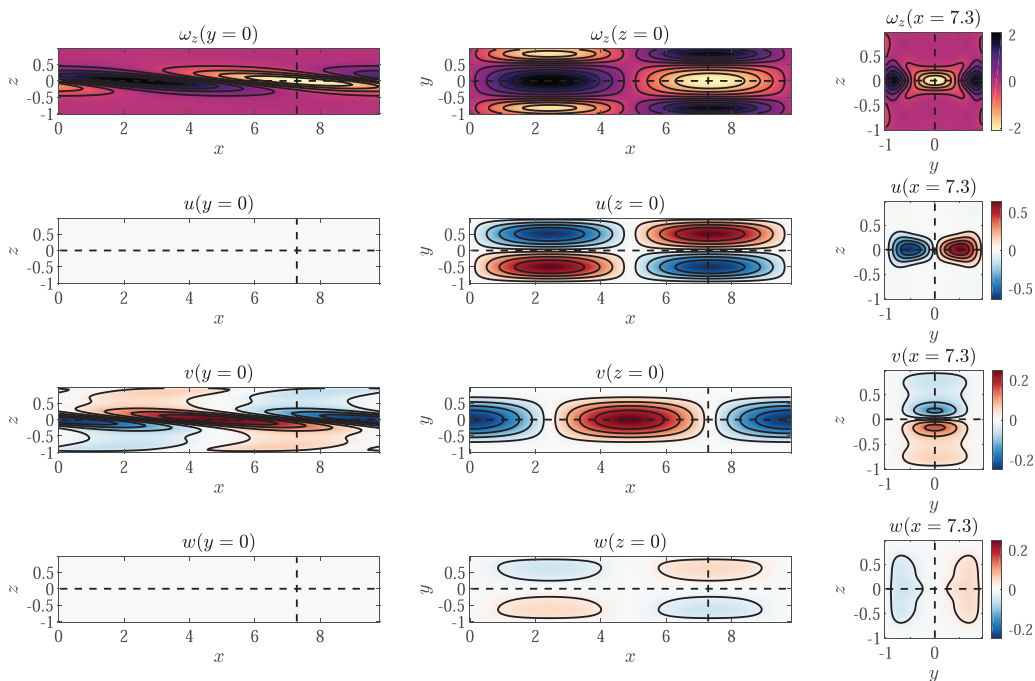
FIG. 10. Some slice views of the KH_T mode shown in Fig. 9. Dashed lines show the locations of the planes in the other columns.

(2) The second effect is that KH_T appears much more sensitive to viscous damping (in the sense that was defined more precisely in Sec. III C) than KH_1 does. As B further decreases, viscous damping becomes more severe, and KH_T is stabilized at a threshold B where KH_1 is still significantly unstable. The KH_T-dominated region is thus shut at $B \approx 0.7$–1.1 (at these values of Re and Ri_b).

From these observations, the KH_T mode appears to be a very delicate instability, in particular because of its ambiguous relation to spanwise confinement. A sufficiently strong confinement can "feed" KH_T (on the condition that Re is not too low) but not without limit: eventually an exceedingly strong confinement can suppress it (due to viscous effects).

B. Increased energy extraction by spanwise confinement

The above observations can be brought together to build an *a posteriori* explanation for the KH_T instability mechanism. Proceeding as in Chap. 7 of Ref. [31], we define the perturbation kinetic energy as

$$K_p = \frac{1}{2} \int_S (\overline{u^2} + \overline{v^2} + \overline{w^2}) dS, \tag{14}$$

where the overbar denotes spatial averaging along x and over an instability period, and $\int_S dS = \int_{-1}^{1} \int_{-B}^{B} dz dy$ the integral over the duct cross section. By manipulating the Navier-Stokes equation and using the boundary conditions, we obtain an evolution equation for the perturbation kinetic energy:

$$\frac{dK_p}{dt} = -\int_S \overline{uw} \frac{\partial U}{\partial z} dS - \int_S \overline{uv} \frac{\partial U}{\partial y} dS - \frac{1}{\mathrm{Re}} \int_S \overline{\|\omega\|^2} dS. \tag{15}$$

(a) KH_1, $Re = 440$, tanh with $\gamma = 5$

(b) KH_T, $Re = 440$, tanh with $\gamma = 5$

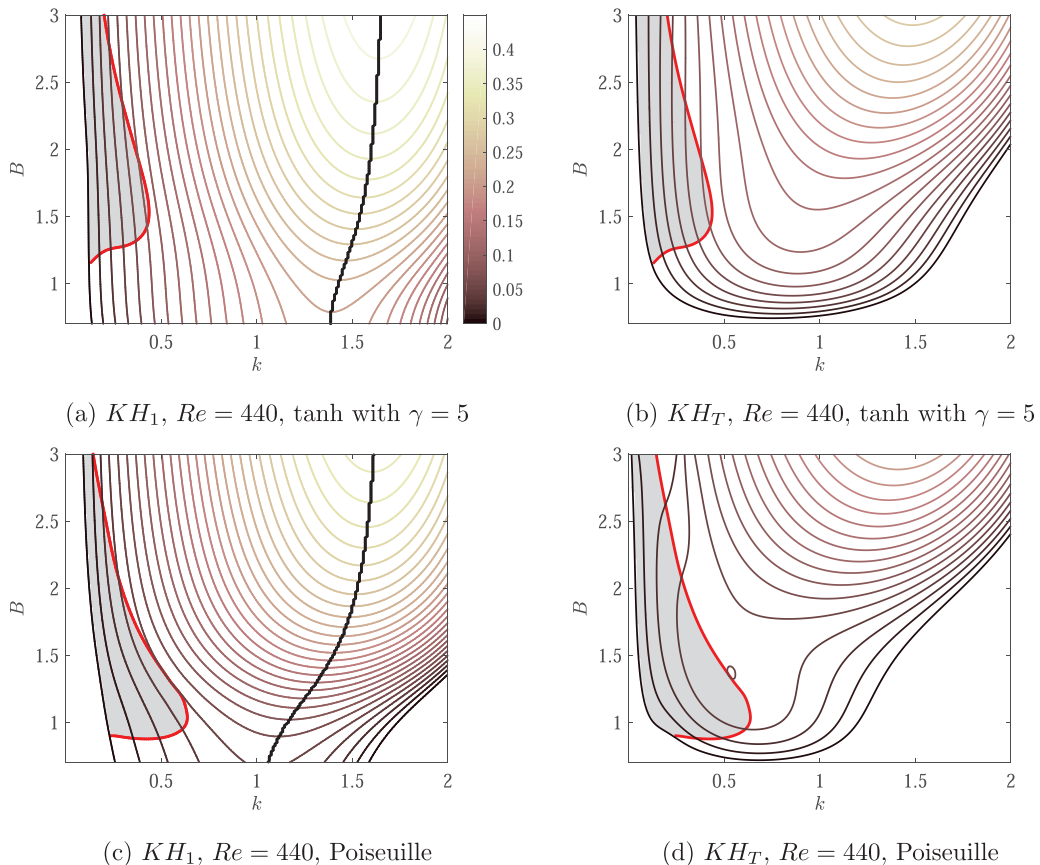(c) KH_1, $Re = 440$, Poiseuille

(d) KH_T, $Re = 440$, Poiseuille

FIG. 11. Growth rates σ_r of KH_1 (left column) and KH_T (right column) in the (k, B) plane for $Re = 440$, $Ri_b = 0$. We compare $M_5(y)$ (top row) to $M_p(y)$ (bottom row). At the left of the red line, inside the gray shaded area KH_T is more unstable than KH_1. The black line is the most unstable growth rate $\sigma_m(B)$ over k.

The last term in $1/Re$ stands for the viscous dissipation and can only induce loss in energy (which does not mean that viscosity has a dissipative effect *only*, since it also affects u, v, w). The first two terms represent the rate of energy transfer, from the z and y mean shear to the perturbations; they may be positive and thus feed the instability. Given two complex fields $a(y, z) \doteq |\hat{a}(y, z)|e^{i\psi_a(y,z)}$ and $b \doteq |\hat{b}(y, z)|e^{i\psi_b(y,z)}$ we can write

$$\overline{ab} = \tfrac{1}{2}|\hat{a}(y, z)||\hat{b}(y, z)| \cos[\phi_a(y, z) - \phi_b(y, z)]e^{2\sigma_r t}. \tag{16}$$

For $t = 0$, we plot in Fig. 12 the two different fields $-\overline{uw}\partial U/\partial z$ and $-\overline{uv}\partial U/\partial y$ computed by Eq. (16): Comparing Figs. 12(a) and 12(b) immediately reveals that both mechanisms contribute to the instability (since they both promote $dK_p/dt > 0$, in red). However, the dominance of the term $-\overline{uw}\partial U/\partial z$ is evident from the scale of the color bar. After performing the cross-section integration, the term in $\partial U/\partial z$ in Eq. (15) is approximately 12 times larger than the one in $\partial U/\partial y$, and is thus primarily responsible for the growth of the instability. The interesting physical implication is that, even if the structure of the KH_T mode differs completely from the KH_1 and 1D KH modes (since its vorticity is principally along z and not along y), it is equally fed by the *spanwise* vorticity of the base flow $\partial U/\partial z$. The positiveness of $[-\int_S \overline{uw}\partial U/\partial z dS]$ is ensured by that fact that $\overline{uw} > 0$ in the whole cross section and $\partial_z U < 0$ such that the main shear transfers energy into the perturbation vortices. This is a consequence of the fact that u and w, concentrated in the region $-0.5 \leqslant u \leqslant 0.5$, are

(a) $-\overline{uw}\partial U/\partial z$

(b) $-\overline{uv}\partial U/\partial y$
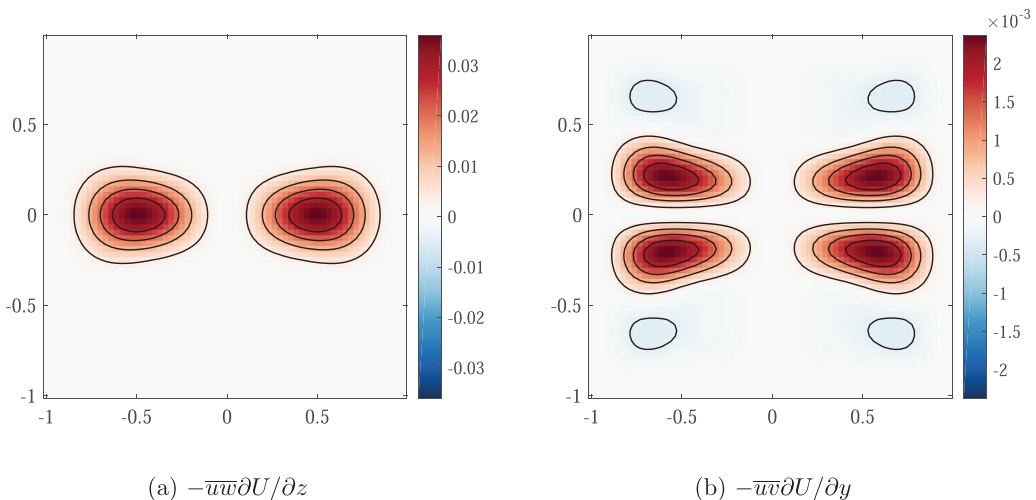
FIG. 12. Energy contribution to the KH_T mode shown in Fig. 9.

almost perfectly in phase. This also means that perturbation vortices are slightly positively sloped along x, and thus feel the main shear $\partial_z U$.

These results suggest that for a very weak stratification ($Ri_b \approx 0$), and strong confinement (small B), a low wavenumber mode (small k) that is intrinsically 2D can unexpectedly become more unstable than the quasi-1D KH_1 wave. This "twisted" KH_T mode may be observed in practice, but only if long waves are preferentially forced.

VI. CONCLUSIONS

In this paper we have compared confined 2D dispersion relations with 1D spanwise-invariant ones, for different aspect ratio B and bulk Richardson numbers Ri_b characterizing the stratified sheared flows in a rectangular duct. In this limited parameter space, the presence of duct walls has a stabilizing effect except in a negligibly small region. Namely, the 1D predictions are almost systematically an upper bound for the 2D growth rates, which decrease monotonically as the lateral walls tighten around the flow. The natural question that arises thus concerns the threshold aspect ratio above which the 1D prediction is relevant. We have shown that the answer is sensitive to the precise structure of the base flow: the thinner the spanwise boundary layers, the lower this minimal aspect ratio. Although less significant, the same conclusion regarding the influence of increasing Ri_b can also be drawn. We have largely restricted ourselves to a particular Ri_b and wavenumber, allowing for a more detailed analysis of the unstable part of the spectrum. In the 2D case, a plethora of unstable modes is observed, and they proliferate as the aspect ratio is increased. These modes present a regularity in their spatial structures, which is perhaps not really all that surprising. Furthermore, from moderate to infinite aspect ratio, the 1D-O dispersion relation for oblique waves seems to be very close to a continuous version of the 2D spectrum, provided the base flow spanwise boundary layer is sufficiently thin. This link is made clear by noticing that, thanks to the spanwise symmetry of the system, the 1D-O dispersion relation also incorporates modes that mimic the same structural regularity as the 2D modes. Here, the quality of the 2D-1D-O alignment is slowly improved by increasing the aspect ratio, and quickly improved by thinning the spanwise boundary layers of the base flow. Implications of these observations are believed to be important. As the confinement widens, the most unstable 2D modes are competing more and more tightly: a slight external forcing on one of their particular wavelength is sufficient to make it emerge preferentially with respect to the one predicted by the 1D analysis. Thus, even in the large aspect ratio limit, the 1D

predictions must be taken with a lot of caution, and should be complemented by a 1D-O analysis. In the 2D context, we expect the mode that oscillates the least in the spanwise direction to be the most unstable one, as a consequence of viscous damping. We have finally shown that, for a very restricted range of parameters, a mode whose spatial structure resembles a "twisted" version of KH_1 (in terms of having dominant crosswise vorticity) becomes more unstable than the classical KH_1 mode. This phenomenon has no 1D counterpart, and is shown to be inherently linked to a tight confinement from which this mode takes advantage. Looking ahead, these results may have interesting implications that could stimulate future research. In line with qualitative comments made in Sec. II, the evolution of the group velocities deduced from Fig. 3 suggests a potential convective-to-absolute transition occurring as the lateral walls are brought closer together. A rigorous saddle-point or impulse response approach would be needed to shed light on the existence of this transition. Such an analysis appears of particular relevance, as in practice the duct is of finite length in the streamwise direction. Thus, it remains unclear if the structure in Ref. [12] is the product of convective instabilities reflected at the extremities of the duct connecting with the reservoirs, or if it would remain self-sustained in an infinite domain. Confinement may play a crucial role in such discrimination, as shown by numerous examples in the literature for unstratified flows (for example, Refs. [23,32,33], among others). In the 2D case, the presence of modes of comparable growth rates could lead to a very rich nonlinear dynamics. This is particularly true considering that these modes are naturally structural harmonics of each other. Thus, the nonlinear creation of higher harmonics of the most unstable one may be strongly amplified and lead to powerful interactions.

APPENDIX A: FORMULATION OF 1D LINEAR STABILITY PROBLEM

The one-dimensional stability problem reduces to solving (for w and ρ)

$$\sigma \begin{bmatrix} \Delta & \\ & \mathcal{I} \end{bmatrix} \begin{bmatrix} w \\ \rho \end{bmatrix} = \begin{bmatrix} \mathcal{L}_w & \mathcal{L}_{w\rho} \\ \mathcal{L}_{\rho w} & \mathcal{L}_\rho \end{bmatrix} \begin{bmatrix} w \\ \rho \end{bmatrix}, \tag{A1}$$

where

$$\mathcal{L}_w = -ikU\Delta + ik\partial_{zz}U + \mathrm{Re}^{-1}\Delta^2,$$
$$\mathcal{L}_{\rho w} = -ikU + (\mathrm{ReSc})^{-1}\Delta,$$
$$\mathcal{L}_{w\rho} = \mathrm{Ri}_b[k^2\cos\theta - ik\sin\theta\partial_z],$$
$$\mathcal{L}_\rho = -\partial_z R,$$

with

$$U(z) = -\sin(\pi z), \quad -1 \leqslant z \leqslant 1, \tag{A2}$$

and

$$\mathcal{R}(z) = -\tanh(2R(z - z_0)), \quad -1 \leqslant z \leqslant 1. \tag{A3}$$

APPENDIX B: FORMULATION OF 1D-OBLIQUE LINEAR STABILITY PROBLEM

This problem corresponds to Eq. (6), after the y dependence of the base flow is removed, and after the ∂_y acting on the perturbations are replaced by $i\beta$. After factorization by v, w, ρ, and p, we end up with the system

$$[\sigma + Uik - \mathrm{Re}^{-1}(-k^2 + \partial_{zz} - \beta^2)]v = -i\beta p,$$
$$[\sigma + Uik - \mathrm{Re}^{-1}(-k^2 + \partial_{zz} - \beta^2)]w = -\partial_z p - \mathrm{Ri}_b\cos(\theta)\rho,$$
$$[\sigma\rho + Uik - (\mathrm{ScRe})^{-1}(-k^2 + \partial_{zz} - \beta^2)]\rho = -(\partial_z R)w,$$
$$[\sigma i\beta - kU\beta - \mathrm{Re}^{-1}(-k^2 i\beta - i\beta^3 + i\beta\partial_{zz})]v$$
$$= [-\sigma\partial_z - ikU\partial_z + ik\partial_z U + \mathrm{Re}^{-1}(-k^2\partial_z - \beta^2\partial_z + \partial_{zzz})]w - k^2 p - ik\mathrm{Ri}_b\sin(\theta)\rho. \tag{B1}$$

v is always multiplied by an odd power of β, when, in the meantime, ρ, w, p, and u (by continuity) are multiplied by an even power of β. Thus, we easily show that the system is invariant under the transformation

$$(\sigma, \beta, u, v, w, \rho) \rightarrow (\sigma, -\beta, Cu, -Cv, Cu, Cw, C\rho), \tag{B2}$$

where $C \in \mathbb{C}$, a constant, is an unimportant consequence of the linearity of the system. Interestingly, v must flip its sign with respect to all the others fields as $\beta \rightarrow -\beta$. The existence of this symmetry has an important consequence. Indeed, by linearity of the system, perturbations of the form

$$\hat{h}(y, z) = \overline{h}(z)e^{i\beta y} + \overline{h}(z)e^{-i\beta y} \doteq \check{h}(z)\cos(\beta y),$$
$$\hat{v}(y, z) = \overline{v}(z)e^{i\beta y} - \overline{v}(z)e^{-i\beta y} \doteq \check{v}(z)\sin(\beta y), \tag{B3}$$

and perturbations of the form

$$\hat{h}(y, z) = \overline{h}(z)e^{i\beta y} - \overline{h}(z)e^{-i\beta y} \doteq \check{h}(z)\sin(\beta y),$$
$$\hat{v}(y, z) = \overline{v}(z)e^{i\beta y} + \overline{v}(z)e^{-i\beta y} \doteq \check{v}(z)\cos(\beta y), \tag{B4}$$

are equally solutions (where $\overline{h}$ denotes any one of u, w, ρ, or p). In other words, they satisfy the 1D-O dispersion relation. This may appear surprising because, although these solutions are periodic in the spanwise direction, they travel purely along the streamwise direction (standing wave), rather than obliquely. We notice that $\check{v}$ is necessarily phase shifted by $i = \sqrt{-1}$ with respect to all the other fields. These solutions could be made more general by adding the same constant phase shift in the harmonic function of $\hat{h}(y, z)$ and $\hat{v}(y, z)$.

APPENDIX C: NUMERICAL METHODS

In the following, we present the numerical methods used for the discretization and solution of the system in Eq. (6). Since our study required us to perform a much greater number of computations than in Ref. [12], we developed a more accurate and faster method than their finite-difference method.

1. Discretizing the equations

Expansions. Equation (6) is discretized by a purpose-built pseudospectral Chebyshev method, together with a crosswise mapping concentrating points at the density interface. The boundary conditions were built directly into the basis functions, so that the eigenfunctions necessarily satisfy the boundary conditions. The perturbation fields are expanded as

$$v(y, z) = \sum_{m=0}^{N_y-1} \sum_{n=0}^{N_z-1} V_{mn}\phi_m(s_y[y])\zeta_n(s_z[z]), \tag{C1a}$$

$$w(y, z) = \sum_{m=0}^{N_y-1} \sum_{n=0}^{N_z-1} W_{mn}\zeta_m(s_y[y])\phi_n(s_z[z]), \tag{C1b}$$

$$\rho(y, z) = \sum_{m=0}^{N_y-1} \sum_{n=0}^{N_z-1} R_{mn}\psi_m(s_y[y])\psi_n(s_z[z]), \tag{C1c}$$

$$p(y, z) = \sum_{m=0}^{N_y-1} \sum_{n=0}^{N_z-1} P_{mn}T_m(s_y[y])T_n(s_z[z]), \tag{C1d}$$

where $T_j(x)$ are the Chebyshev polynomials of order j.

Basis functions. The three sets of functions $\zeta_j(x)$, $\psi_j(x)$, and $\phi_j(x)$ respectively satisfy Dirichlet, Neumann, and Dirichlet-Neumann boundary conditions at $x = \pm 1$, $\forall j$. Classically, they are well-chosen linear combinations of Chebyshev polynomials. Expressions for such functions were proposed, e.g., in Ref. [34], which have been checked to be suitable in the present case too. However, a well-known disadvantage of Chebyshev polynomials is their intense (and high-frequency) oscillations near boundaries, dangerously blowing up with the order of differentiation: $|d^p T_N(\pm 1)/dx^p| \sim N^{2p}$ [35]. As the present problem contains derivatives up to third order (through the terms $\partial_{yyy} v$ and $\partial_{xxx} w$), the corresponding discretization matrices may inherit an $O(N^6)$ condition number, which could become particularly challenging for fine grids. To overcome this problem, we adopt the method proposed by Heinrichs [36]:

$$\zeta_j(x) = (1 - x^2) T_j(x),$$
$$\phi_j(x) = (1 - x^2)^2 T_j(x),$$

where we easily check that $\zeta(\pm 1) = \phi(\pm 1) = \phi'(\pm 1) = 0$. In the pth derivative of $\zeta_j(x)$, the prefactor $1 - x^2$ kills the $d^p T_j/dx^p$ term at $x = \pm 1$, leading to a new condition number $O(N^{2(p-1)})$. The same applies to $\phi_j(x)$, $d^p T_j/dx^p$, and $d^{p-1} T_j/dx^{p-1}$, leading to a condition number $O(N^{2(p-2)})$. Therefore, our discretization matrices are at worst $O(N^2)$ for both ζ's (up to second-order derivative) and ϕ's (up to third-order one). For ψ's, which are only used in the density perturbation expansion, we adopted the expression proposed by Ref. [35]:

$$\psi_{2n}(x) = \begin{cases} 1, & n = 0 \\ T_{2n}(x) - \left[\frac{n^2}{(n+1)^2}\right] T_{2n+2}(x), & n = 1, 2, \ldots, \end{cases}$$

$$\psi_{2n+1}(x) = T_{2n+1}(x) - \left[\frac{2n+1}{2n+3}\right]^2 T_{2n+3}(x), \quad n = 0, 1, \ldots,$$

where $\psi'(\pm 1) = 0$.

Collocation points. We chose "Gauss-Chebyshev" collocation points, equivalent to the roots of the Chebyshev polynomials:

$$s_y = \cos\left[\frac{(2i-1)\pi}{2N_y}\right], \quad s_z = \cos\left[\frac{(2i-1)\pi}{2N_z}\right], \tag{C2}$$

where s_y and s_z designate respectively the spanwise and crosswise (vertical) collocation points. This choice contrasts with the classical "Gauss-Lobatto" discretization, and excludes boundary points. This is deliberate in order to avoid spurious pressure modes, inherent to Gauss-Lobatto meshing. If boundary points are needed, for instance with the use of the τ method, the $\mathbb{P}_N - \mathbb{P}_{N-2}$ technique presented in Ref. [37] is a suitable alternative. Because it relies on the interpolation of the pressure field, it however excludes all nonlinear mapping. Indeed the Gauss-Lobatto points locations, optimal for a polynomial interpolation, are then distorted and the Runge phenomena is observed at the boundaries, precisely where we desire the pressure values.

Coordinate mapping. Under mapping transformations, the physical points corresponding to the numerical grid of Eq. (C2) are recovered as

$$y = g_y(s_y) = A s_y,$$
$$z = g_z(s_z; \alpha_1, \alpha_2) = \alpha_2 + \frac{\tan[(s_z - s_0)\lambda]}{\alpha_1},$$

where

$$s_0 = \frac{\kappa - 1}{\kappa + 1}, \quad \kappa = \frac{\arctan(\alpha_1(1 + \alpha_2))}{\arctan(\alpha_1(1 - \alpha_2))}, \quad \lambda = \frac{\arctan(\alpha_1(1 - \alpha_2))}{(1 - s_0)}.$$

The simple linear mapping g_y transforms the interval $y \in [-A, A]$ into $s_y \in [-1, 1]$, where the Chebyshev polynomials are defined. The mapping g_z (see Ref. [38]), concentrates the collocation

points around $z = \alpha_2$ with a strength modulated by α_1. As a sharp evolution of the density perturbation is expected at the interface, we set $\alpha_2 = z_0$. An optimum for α_1 can be found through the technique proposed in Ref. [38]. However, the present problem is slightly different since the mapping also impacts on the velocity: a compromise was found by trial and error to obtain an α_1 sufficiently big as to smooth out the density, but sufficiently small as not to distort the velocity substantially. Overall, this crosswise mapping sped up the convergence impressively.

As mentioned in Ref. [35], despite the use of mappings, the whole problem can still be solved numerically solely in terms of physical variables and grid. In the code, this requires two additional subroutines that (i) compute the physical points from Eq. (C2) and (ii) perform the chain rule to transform s derivatives into z ones. These pivoting expressions are analytically expressed as

$$\frac{d}{dz} = \left(\frac{1}{g_1}\right)\frac{d}{ds},$$

$$\frac{d^2}{dz^2} = \frac{1}{g_1^3}\left(g_1\frac{d^2}{ds^2} - g_2\frac{d}{ds}\right),$$

$$\frac{d^3}{dz^3} = \frac{1}{g_1^5}\left[g_1^2\frac{d^3}{ds^3} - 3g_1 g_2\frac{d^2}{ds^2} + \left(-g_3 g_1 + 3g_2^2\right)\frac{d}{ds}\right],$$

$$\frac{d^4}{dz^4} = \frac{1}{g_1^7}\left[g_1^3\frac{d^4}{ds^4} - 6g_2 g_1^2\frac{d^3}{ds^3} + \left(-4g_3 g_1^2 + 15g_2^2 g_1\right)\frac{d^2}{ds^2} + \left(-g_4 g_1^2 + 10g_3 g_2 g_1 - 15g_2^3\right)\frac{d}{ds}\right],$$

where we use the following shorthand notation for derivatives: $g_1 = g'(s)$, $g_2 = g''(s)$, $g_3 = g'''(s)$, and $g_4 = g''''(s)$. For the s derivatives, the chain rule must also be used to transform the T derivatives into ζ and ϕ ones (analytical expression in Ref. [35]). In order to illustrate the discretization machinery, the $\mathcal{L}_v$ operator becomes

$$\mathbf{L}^v = -ik\mathbf{U} + \mathrm{Re}^{-1}\left(-k^2\mathbf{I}^v + \mathbf{D}_{yy}^v + \mathbf{D}_{zz}^v\right),$$

with

$$\mathbf{I}^v = \mathbf{D}_{0,y}^v \otimes \mathbf{D}_{0,z}^v, \quad \mathbf{D}_{yy}^v = \mathbf{D}_{2,y}^v \otimes \mathbf{D}_{0,z}^v, \quad \text{and} \quad \mathbf{D}_{zz}^v = \mathbf{D}_{0,y}^v \otimes \mathbf{D}_{2,z}^v.$$

In addition, we express as in a 1D problem:

$$\left[\mathbf{D}_{0,y}^v\right]_{ij} = \frac{d\phi_j(y_i)}{dy}, \quad \left[\mathbf{D}_{2,y}^v\right]_{ij} = \frac{d^2\phi_j(y_i)}{dy^2}, \quad \left[\mathbf{D}_{0,z}^v\right]_{ij} = \frac{d\zeta_j(z_i)}{dz}, \quad \text{and} \quad \left[\mathbf{D}_{2,z}^v\right]_{ij} = \frac{d^2\zeta_j(z_i)}{dz^2}.$$

Processing similarly for all operators results in a new generalized eigenvalue problem:

$$\sigma\mathbf{B}x = \mathbf{A}x, \tag{C3}$$

where $x = [\mathbf{V}, \mathbf{W}, \mathbf{R}, \mathbf{P}]$, and where $\mathbf{A}$ and $\mathbf{B}$ are $(4NyNz) \times (4NyNz)$ matrices.

2. Solving the discrete system

Provided k ($\in\mathbb{R}$), and a "shift" μ ($\in\mathbb{C}$) close to where the eigenvalue is sought, the system of Eq. (C3) is solved for σ ($\in\mathbb{C}$) using the shift and invert algorithm. The selected eigenvalue among the full spectrum is that nearest to μ. The procedure detailed in Ref. [13] is followed, except that we preferred a QR decomposition to their LU decomposition for reasons of numerical stability. In particular, the shift and inverted matrix $\mathbf{K} = (\mathbf{A} - \mu\mathbf{B})^{-1}\mathbf{B}$ is computed as

$$\mathbf{QR} = \mathbf{A} - \mu\mathbf{B}, \tag{C4a}$$

$$\mathbf{C} \doteq \mathbf{Q}^{-1}\mathbf{B} = \mathbf{Q}^T\mathbf{B}, \tag{C4b}$$

$$\mathbf{K} = \mathbf{R}^{-1}\mathbf{C}, \tag{C4c}$$

where the decomposition in Eq. (C4a), as well as the inversion in Eq. (C4c), are respectively performed by [Q,R] = qr(A-mu*B) and K = R\C commands in MATLAB. Still following terminology in Ref. [13], the generalized eigenvalue problem (C3) can be rewritten as a standard one:

$$\mathbf{K}\boldsymbol{x} = \theta\boldsymbol{x}, \tag{C5}$$

where $\theta = (\sigma - \mu)^{-1}$. It is solved using the implicitly restarted Arnoldi method embedded in MATLAB's function eigs, together with the lm (largest magnitude) option. Choosing this option ensures that the selected eigenvalue maximizes the quantity $\|\theta\| = \|(\sigma - \mu)^{-1}\|$, thus minimizing the distance between σ and μ. Sometimes, the full spectrum is of interest, in particular when an initial guess for μ is sought. In this case, the QZ algorithm is used directly for the eigenvalues of Eq. (C3) through MATLAB's function eig(A,B).

---

[1] W. R. Geyer, C. Lavery, E. Scully, and J. H. Trowbridge, Mixing by shear instability at high Reynolds number, Geophys. Res. Lett. **37**, L22607 (2010).

[2] W. D. Smyth and W. Peltier, Instability and transition in finite-amplitude Kelvin-Helmholtz and Holmboe waves, J. Fluid Mech. **228**, 387 (1991).

[3] W. D. Smyth, J. R. Carpenter, and G. A. Lawrence, Mixing in symmetric Holmboe waves, J. Phys. Oceanogr. **37**, 1566 (2007).

[4] J. R. Carpenter, G. A. Lawrence, and W. D. Smyth, Evolution and mixing of asymmetric Holmboe instabilities, J. Fluid Mech. **582**, 103 (2007).

[5] H. Salehipour, C. P. Caulfield, and W. R. Peltier, Turbulent mixing due to the Holmboe wave instability at high Reynolds number, J. Fluid Mech. **803**, 591 (2016).

[6] H. Salehipour, W. R. Peltier, and C. P. Caulfield, Self-organized criticality of turbulence in strongly stratified mixing layers, J. Fluid Mech. **856**, 228 (2018).

[7] K. Smith, C. P. Caulfield, and J. R. Taylor, Turbulence in forced stratified shear flows, J. Fluid Mech. **910**, A42 (2021).

[8] C. P. Caulfield, W. R. Peltier, S. Yoshida, and M. Ohtani, An experimental investigation of the instability of a shear-flow with multilayered density stratification, Phys. Fluids **7**, 3028 (1995).

[9] E. W. Tedford, R. Pieters, and G. A. Lawrence, Symmetric Holmboe instabilities in a laboratory exchange flow, J. Fluid Mech. **636**, 137 (2009).

[10] J. R. Carpenter, E. Tedford, M. Rahmani, and G. A. Lawrence, Holmboe wave fields in simulation and experiment, J. Fluid Mech. **648**, 205 (2010).

[11] C. R. Meyer and P. F. Linden, Stratified shear flow: Experiments in an inclined duct, J. Fluid Mech. **753**, 242 (2014).

[12] A. Lefauve, J. L. Partridge, Q. Zhou, S. B. Dalziel, C. P. Caulfield, and P. F. Linden, The structure and origin of confined Holmboe waves, J. Fluid Mech. **848**, 508 (2018).

[13] J. Hu, D. Henry, X. Yin, and H. BenHadid, Linear biglobal analysis of Rayleigh-Bénard instabilities in binary fluids with and without throughflow, J. Fluid Mech. **713**, 216 (2012).

[14] J. Cudby and A. Lefauve, Weakly nonlinear Holmboe waves, Phys. Rev. Fluids **6**, 024803 (2021).

[15] J. R. Carpenter, E. W. Tedford, E. Heifetz, and G. A. Lawrence, Instability in stratified shear flow: Review of a physical interpretation based on interacting waves, Appl. Mech. Rev. **64**, 060801 (2011).

[16] L. M. Hocking, Nonlinear instability of flow in a rectangular pipe with large aspect ratio, Z. Angew. Math. Phys. **29**, 100 (1978).

[17] T. Tatsumi and T. Yoshimura, Stability of the laminar flow in a rectangular duct, J. Fluid Mech. **212**, 437 (1990).

[18] V. Theofilis, P. W. Duck, and J. Owen, Viscous linear stability analysis of rectangular duct and cavity flows, J. Fluid Mech. **505**, 249 (2004).

[19] R. J. Briggs, *Electron-Stream Interaction with Plasmas* (MIT Press, Cambridge, MA, 1964).

[20] A. Bers, *Linear Waves and Instabilities* (Gordon and Breach, New York, 1975), p. 117.

[21] P. Huerre and P. A. Monkewitz, Local and global instabilities in spatially developing flows, Annu. Rev. Fluid Mech. **22**, 473 (1990).

[22] P. Carrière and P. Monkewitz, Convective versus absolute instability in mixed Rayleigh-Bénard-Poiseuille convection, J. Fluid Mech. **384**, 243 (1999).

[23] M. P. Juniper, The effect of confinement on the stability of two-dimensional shear flows, J. Fluid Mech. **565**, 171 (2006).

[24] P. Brancher and J. M. Chomaz, Absolute and Convective Secondary Instabilities in Spatially Periodic Shear Flows, Phys. Rev. Lett. **78**, 658 (1997).

[25] I. Delbende and J.-M. Chomaz, Nonlinear convective/absolute instabilities in parallel two-dimensional wakes, Phys. Fluids **10**, 2724 (1998).

[26] I. Delbende, J.-M. Chomaz, and P. Huerre, Absolute/convective instabilities in the Batchelor vortex: A numerical study of the linear impulse response, J. Fluid Mech. **355**, 229 (1998).

[27] F. Gallaire and J.-M. Chomaz, Mode selection in swirling jet experiments: A linear stability analysis, J. Fluid Mech. **494**, 223 (2003).

[28] H. B. Squire, On the stability of three-dimensional disturbances of viscous flow between parallel walls, Proc. R. Soc. London A **142**, 621 (1933).

[29] W. D. Smyth and W. R. Peltier, Three-dimensional primary instabilities of a stratified, dissipative, parallel flow, Geophys. Astrophys. Fluid Dyn. **52**, 249 (1990).

[30] P. J. Schmid and D. S. Henningson, *Stability and Transition in Shear Flows* (Springer, Berlin, 2012).

[31] *Hydrodynamics and Nonlinear Instabilities*, Collection Alea-Saclay: Monographs and Texts in Statistical Physics, edited by C. Godrèche and P. Manneville (Cambridge University Press, Cambridge, UK, 1998).

[32] J. J. Healey, Destabilizing effects of confinement on homogeneous mixing layers, J. Fluid Mech. **623**, 241 (2009).

[33] S. J. Rees and M. P. Juniper, The effect of confinement on the stability of viscous planar jets and wakes, J. Fluid Mech. **656**, 309 (2010).

[34] Y. Kato and K. Fujimura, Prediction of pattern selection due to an interaction between longitudinal rolls and transverse modes in a flow through a rectangular channel heated from below, Phys. Rev. E **62**, 601 (2000).

[35] J. Boyd, *Chebyshev and Fourier Spectral Methods*, 2nd ed. (Dover, New York, 2000).

[36] W. Heinrichs, A stabilized treatment of the biharmonic operator with spectral method, J. Sci. Stat. Comput. **12**, 1162 (1991).

[37] R. Peyret, *Spectral Methods for Incompressible Viscous Flow* (Springer, Berlin, 2002).

[38] A. Bayliss, Mappings and accuracy for Chebyshev pseudo-spectral approximations, J. Comput. Phys. **101**, 349 (1992).